COHERENT CONTROL OVER STRONG-FIELD DISSOCIATION OF HETERONUCLEAR DIATOMIC MOLECULES

by

Brandon Rigsbee

B.S., San Diego State University, 2011

A DISSERTATION

submitted in partial fulfillment of the
requirements for the degree

MASTER OF SCIENCE

Department of Physics
College of Arts and Sciences

KANSAS STATE UNIVERSITY
Manhattan, Kansas

2015

Approved by:

Major Professor
Brett Esry

Copyright

Abstract

In the last 20 years, advancements in laser technology have allowed for the production of intense laser pulses with durations in the femtosecond (10^{-15} second) regime, giving scientists the ability to probe nuclear dynamics on their natural time scale. Study of the dissociated fragments created by these intense fields can be used to learn about the molecular structure and dynamics. The work presented in this thesis focuses on controlling this light–molecule interaction in such a way that we can preferentially dissociate the molecule to a desired final product. The hydrogen molecular ion, HD^+, as well as LiF serve as simple systems that can be studied theoretically for a broad range of laser parameters. Our goal in using these relatively simple systems is to capture the essential physics of the light–molecule interaction and develop general methods to describe these interactions in more complex systems.

Table of Contents

List of Figures

List of Tables

Chapter 1

Introduction

From determining the colors we see to the formation of the known universe, the interaction of light with matter is integral to all facets of life. It is no surprise that these interactions have garnered the interest of scientists—making them an intensely studied subject for a long time. The study of black body radiation using absorption and emission spectra allowed scientists to identify the composition of stars and other celestial bodies. Study of the photoelectric effect, the ejection of electrons from a metal surface when exposed to light, led to the invention of the photon in order to match theory to experimental results. These studies, in addition to many others, eventually led to the birth of quantum mechanics in the early 1900s. In the 1950s, the invention of the laser, a collimated beam of coherent light with a narrow range of frequencies, gave scientists a new tool to probe atomic and molecular structure that is used in many fields of physics today.

With recent advances in laser technology, we now have the ability to generate intense pulses of light that are in the femtosecond (10^{-15} second) regime—the natural time scale for nuclear motion in molecules. The work presented in this thesis focuses on studying the response of simple, diatomic molecules when exposed to these laser pulses. Ahmed Zewail, the father of femtochemistry, won the 1999 Nobel Prize in Chemistry for his pioneering

efforts to measure molecular structure and dynamics using a pump-probe method in the femtosecond regime [2]. Since these first experiments, further advances in technology have allowed this field of research to progress by offering the ability to generate a wider variety of pulses with the trend going toward generating few-cycle-long pulses with higher intensities. The titanium-sapphire laser is one of the most commonly used in ultrafast science and generates pulses with intensities of 10^{13}–10^{16} W/cm^2 with a central frequency around 800 nm. These parameters lead to high-order, nonlinear processes in diatomic molecules that are challenging to describe theoretically. Understanding this light-molecule interaction is key to learning about the structure and dynamics of molecules.

One of the many applications of ultrafast laser pulses is in the field of coherent control where the goal is to manipulate the dynamics of the light-molecule reaction. This control comes from the interference of different quantum pathways and is achieved by shaping the laser pulse. For example, one may seek to control the yield of the final products of molecular dissociation via the pulse duration. The key is determining what properties of the laser are most important in the reaction. There are different philosophies governing the selection of the laser properties that give the best control. Some choose to use a pulse shaper controlled by a genetic algorithm as a sophisticated, but "brute-force" method to achieve the desired control [3]. Another method is to use the molecular structure and general knowledge of laser-molecule interactions to identify possible interfering pathways and devise a laser field that creates and manipulates the interference of these pathways [4].

The majority of theoretical work in this field is based on finding numerical solutions of the time-dependent Schrödinger equation (TDSE). A general, full-dimensional TDSE for a diatomic molecule in a strong field is an extremely challenging problem that has not been rigorously solved because it involves solving n coupled, differential equations where n is the infinite number of electronic states of the molecule. The Born-Oppenheimer approximation [5] has become the standard method to treat such systems in the ultrafast community.

This is an adiabatic approximation where it is recognized that the time scale for electronic motion is much smaller than for nuclear motion and can be, approximately, separated—decoupling the equations, in the absence of an external field, one must solve. Further approximation is made by reducing the number of electronic channels included in the calculation, thereby reducing the number of differential equations required to solve the system. This means that ionization of the molecule is typically neglected along with many of the high-energy electronic states. The limitation of, and modification to, these approximations will be discussed in the following chapters.

The goal of the work presented in this thesis is to study the dissociation of heteronuclear, diatomic molecules using intense, ultrafast fields. The results are limited to the hydrogen molecular ion, HD^+, and LiF, but the hope is to be able to explain our findings in a general way that can be applied to other systems. A more detailed introduction is provided in each chapter to give more context to and outline the goals of the calculations. The common thread between all chapters is that we wish to influence the final products of dissociation using the laser field. We use our knowledge of the molecular structure and the basic principles of quantum mechanics to generate control schemes in an attempt to gain maximum control over the final yields.

1.1 Outline

In this thesis, we will examine control over the dissociation yields in diatomic molecules using a variety of different laser pulses. In chapter 2, I will discuss the general theory used throughout the following chapters. This covers the solutions to the Schrödinger equation including the spatial representation and time propagation method used. Chapter 3 explores the dissociation of HD^+ in intense fields with varying wavelengths. One goal is to determine the role of the permanent dipole moment in the dissociation dynamics. Chapter 4 also

discusses the dissociation of HD^+, but now in the context of controlling the yields via the carrier-envelope phase (CEP) of the laser pulse. The pulse durations are much shorter relative to those in chapter 3 where the CEP plays no role. Here, we will cover the general theory that describes the CEP-dependence of observables and use it to learn more about our results. In chapter 5, we move our focus to LiF which exhibits much richer electronic structure. We employ a pump-probe scheme to better take advantage of the properties of the molecule to gain much better coherent control over the dissociation yields.

Chapter 2

Theory and Numerical Methods

The work presented in this thesis is focused on controlling the outcome of strong-field dissociation of heteronuclear molecules. Naturally, the general approach to solving these systems is very similar. In particular, the solutions to the time-dependent Schrödinger equation and its energy analysis are common threads between all studies. The goal of this chapter will provide the theoretical and numerical framework used in the remainder of the thesis.

2.1 Time-Dependent Schrödinger Equation

The work presented here relies on accurate solutions to the time-dependent Schrödinger equation (TDSE) in the Born-Oppenheimer basis [5, 6] (atomic units are used throughout unless specified otherwise),

$$i\frac{\partial}{\partial t}\mathbf{F}(R,t) = \Big[\mathbf{H}_0(R) + \mathbf{V}(R,t)\Big]\mathbf{F}(R,t), \tag{2.1}$$

where $\mathbf{H}_0(R)$ is the field-free Hamiltonian, $\mathbf{V}(R,t)$ describes the interaction with the laser field, and $\mathbf{F}(R,t)$ is the multichannel, radial wavefunction. The solutions to the TDSE

thus include nuclear vibration and electronic excitation, but exclude ionization and nuclear rotation. The physical processes and observables we wish to examine in this thesis are not expected to heavily depend on nuclear rotation. The exclusion of nuclear rotation allows us to use a simplified calculation that can still provide a qualitative understanding of the systems studied. To avoid any errors from not including ionization, we limit our intensity to regimes where the ionization is expected to be negligible [7, 8]. In the case of HD^+, the wavelengths used in this work fall into the near-to-mid-IR regime which allows us to consider only a few electronic states because the population in the higher manifolds is expected to be negligible [9]. While the study described in Ref. [9] is for H_2^+, the relative energy spacing between the $n = 1$ and $n = 2$ manifolds and the population in the excited manifold is expected to be similar for HD^+. The number of states one must include is entirely dependent on the electronic structure. In the case of both HD^+ and LiF, only the lowest two electronic states need to be included in our calculations. This means that the radial wavefunction take the form

$$\mathbf{F}(R,t) = \begin{pmatrix} F_1(R,t) \\ F_2(R,t) \end{pmatrix}, \tag{2.2}$$

where $F_1(R,t)$ and $F_2(R,t)$ are the radial wavefunctions on a single electronic channel.

The general expression [6, 10] for the adiabatic, field-free Hamiltonian is

$$\mathbf{H}_0(R) = -\frac{1}{2\mu}\left(\mathbf{I}\frac{\partial^2}{\partial R^2} + \mathbf{P}(R)\frac{\partial}{\partial R} + \frac{\partial}{\partial R}\mathbf{P}(R) + \mathbf{Q}(R)\right) + \mathbf{U}(R), \tag{2.3}$$

where μ is the reduced mass, $\mathbf{I}$ is the unit matrix, $\mathbf{U}(R)$ is the diagonal matrix of the adiabatic electronic potentials, and $\mathbf{P}(R)$ and $\mathbf{Q}(R)$ are the non-adiabatic coupling elements. The off-diagonal elements of $\mathbf{P}$ and $\mathbf{Q}$ describe the coupling of the radial and electronic degrees of freedom that drive non-radiative transitions between electronic states. These

couplings create additional dissociation pathways that give more or fewer opportunities to control the final products. Using HD^+ as an example, the couplings allow transfer between the $1s\sigma$ and $2p\sigma$ electronic states that may not be possible at some laser parameters meaning that more pathways are available to manipulate to control the final yields. However, it turns out that the same coupling mixes the channels equally for a large range of laser parameters meaning that control over the final products is more difficult than one might expect. The method used to calculate all matrix elements depends on the system being treated and will be described in detail for each case.

The laser-molecule interaction is

$$\mathbf{V}(R,t) = -\mathbf{D}(R)\mathcal{E}(t), \tag{2.4}$$

where $\mathbf{D}(R)$ is the dipole matrix which includes both permanent and electronic dipole terms, and $\mathcal{E}(t)$ is the electric field. This formulation of the laser-molecule interaction relies on the dipole approximation of the electric field and uses the length gauge. The use of the dipole approximation is justified by the fact that we use wavelengths much larger than the molecule we study [5]. In general, we use pulses in the femtosecond regime that have a Gaussian envelope. The pulse duration is chosen such that the DC component, calculated by time-integration of the electric field, is negligible.

2.2 Numerical Methods

2.2.1 Basis Splines

For the work presented here, a basis-spline (b-spline) representation for the radial coordinate, R, was used. A discussion of the use of b-splines to solve the Schrödinger equation has already been outlined previously [11], so we will focus on the basic ideas here.

The radial wavefunction can be expressed as a linear combination of b-splines:

$$\mathbf{F}(R,t) = \sum_n \mathbf{c}_n(t) u_n(R). \tag{2.5}$$

Here, $\mathbf{c}_n$ are the coefficients and $u_n(R)$ is the corresponding b-spline. The plot of b-splines as a function of R is shown in Fig. 2.1 as an example. The splines are defined on the grid we choose and are nonzero for a small subset of R. They are continuous for $k-1$ derivatives, where k is the order of the b-splines—giving our wavefunctions a high degree of smoothness. The values of $u_n(R)$ at edges of the box depend on the boundary conditions we impose on the system. In the example shown in the figure, the splines satisfy the boundary condition that the wavefunction goes to zero at the boundaries of the box.

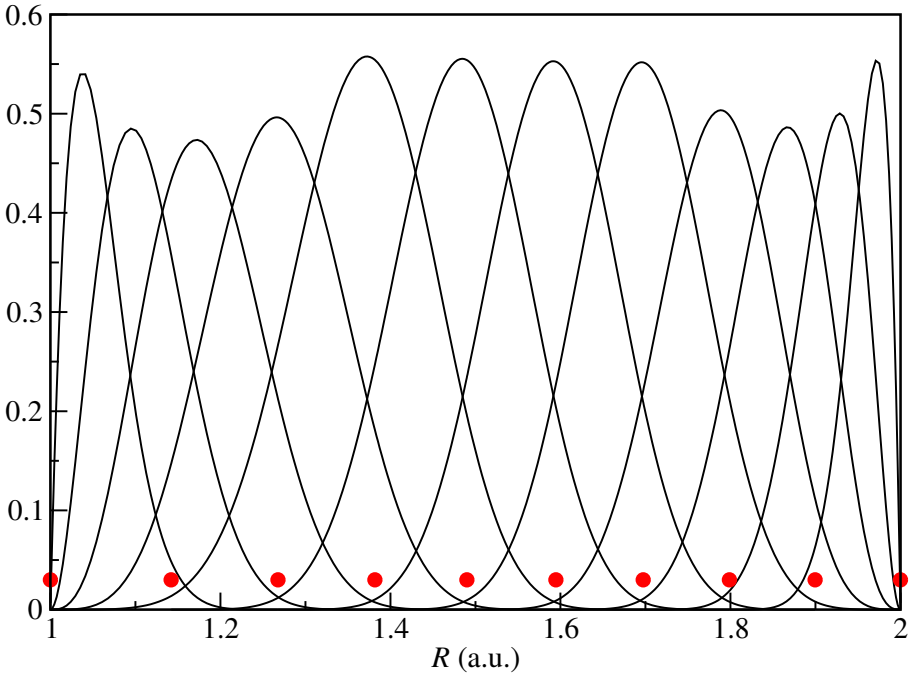

Figure 2.1: *Sample plot of b-splines, $u_n(R)$, for $1 \leq R \leq 2$. The splines satisfy the boundary conditions $F(1) = F(2) = 0$. The red dots represent the spatial grid the splines were based on.*

After combining Eq. (2.1) and (2.5), we can project out $u_n(R)$ and get the TDSE in

terms of the b-spline coefficients:

$$i\mathbf{O}\frac{d}{dt}\mathbf{c} = \mathbf{H}\mathbf{c}, \tag{2.6}$$

where $\mathbf{O}$ is the overlap matrix. In addition, the Hamiltonian and overlap are symmetric, banded matrices that are, numerically, convenient for use with LAPACK [12] subroutines. The drawback to using b-splines is that they form a nonorthogonal basis which means that the overlap matrix must be calculated and more operations are required in a typical calculation in comparison to other methods such as FEDVR [13].

2.2.2 WKB Grid

The distribution of spatial points has a large impact on the efficiency and convergence of a given calculation. While a grid with linear spacing is a safe choice when approaching any calculation, it is often inefficient. We use the WKB (Wentzel, Kramers, and Brillouin) approximation to use the electronic structure to dictate the grid distribution.

The local momentum of the wavefunction is calculated for a specified maximum energy and is used to determine the required density of points in that region. The result is a non-uniform grid that has a larger density of points where the wavefunction is expected to have fast oscillations (near the potential well) and fewer points where the wavefunction is slowly varying (large R). This can be seen explicitly in Fig. 2.2 where fewer points are needed at larger internuclear distances giving it a clear advantage over a linear distribution.

2.2.3 Lanczos Propagator

There are many methods available to time evolve the wavefunction. It is important to choose a scheme that works accurately and efficiently for the system being studied. In the work presented here, the Arnoldi-Lanzcos propagation scheme is employed [14]. This is an explicit method that naturally preserves the norm of the wavefunction during propagation.

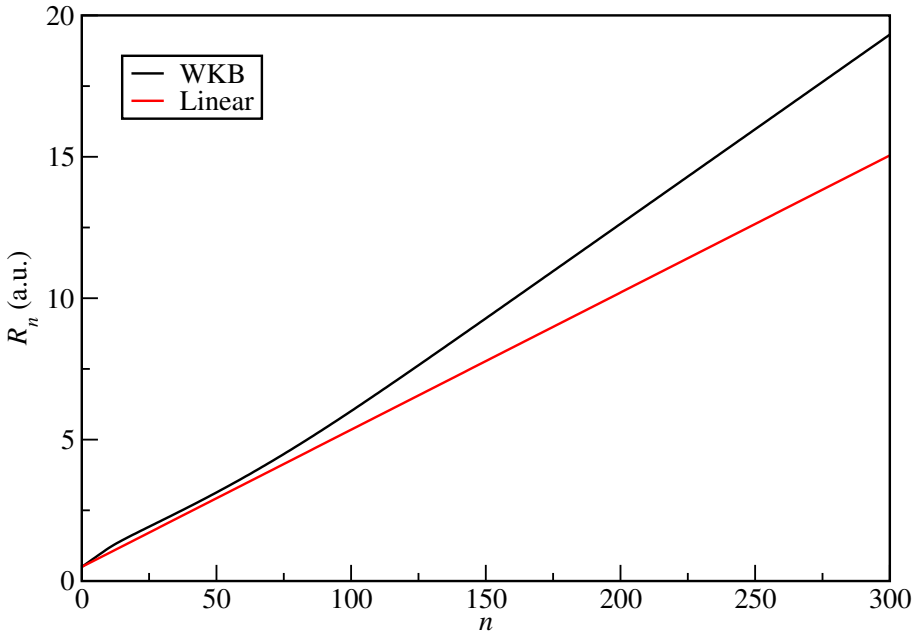

Figure 2.2: *Sample grid distribution for HD^+ using WKB with a maximum kinetic energy of 0.1 a.u. The red line represents a linear grid distribution that would give a similar level of convergence.*

In addition, it is well suited to handle nonorthogonal basis sets with minimal adjustments to the typical formulation. A full derivation of the propagation with a nonorthogonal basis is outlined by Guan *et al.* [14] and references therein.

The Lanczos algorithm is based on the construction of a Krylov subspace of order n that is built of repeated matrix-vector multiplications of the Hamiltonian and wavefunction. The error associated with this scheme depends on both the time step, Δt, and the size of the Krylov subspace. Increasing the time step means that a larger subspace is required. Conversely, decreasing the time step allows the use of a smaller subspace. In our code, we specify Δt and an error tolerance and then increase the size of the subspace until the error is below our tolerance. In this way, we ensure that our solutions are always accurate and we can adjust the time step to find the most efficient calculation for a given set of laser parameters.

2.3 Observables

For any calculation performed, we must compute the physical observables if we wish to have any discussion of the physics and compare to experiments. Since we do not include nuclear rotation in our calculations, we are limited to a few observables that are relevant to ultrafast studies. The most common of these are the energy differential dissociation probability and the total dissociation yields.

The differential dissociation probability in a given channel, i, is expressed as

$$\frac{dP_i}{dE} = \left| \left\langle \mathbf{F}_{i,E}^{(-)} \middle| \mathbf{F} \right\rangle \right|^2 . \tag{2.7}$$

Here, $\mathbf{F}_{i,E}^{(-)}$ are the multichannel scattering states, and $\mathbf{F}$ are the solutions of the TDSE. The calculation of the scattering states will be detailed in the following section. Integrating Eq. (2.7) over energy gives the total dissociation probability for a given channel, P_i. It is important to note that this formulation is only for a single orientation of the molecule.

Sometimes it can be beneficial to look at the total dissociation yield of a single channel compared to the total dissociation probability from all included channels. This quantity is known as the branching ratio:

$$\mathcal{B}_i = \frac{P_i}{\sum_i P_i}. \tag{2.8}$$

This quantity explicitly shows the importance of a single dissociation channel relative to the other channels included. For the work in this thesis, we will be focused on learning how these branching ratios change with the parameters of our laser and what physical mechanisms are involved with the final goal being to develop control schemes to efficiently control the final products in these light-matter interactions.

2.4 Energy Analysis

An energy analysis of our solutions to the TDSE allows us to calculate physical observables that can then be compared to experimental results. This analysis is performed by projecting the solution of the TDSE after time propagation onto scattering states. These scattering states describe energy-normalized wavefunctions that are outgoing on a single dissociation channel. We use a well-established R-matrix method to compute these states [15]. The process begins by solving an eigenvalue problem for the log derivatives, $\mathbf{b}$, of the wavefunction,

$$2\mu \left(E\mathbf{O} - \mathbf{H}_0\right) \mathbf{F}_E = \mathbf{b}\mathbf{F}_E, \tag{2.9}$$

where E is a given energy of the system, $\mathbf{F}_E$ are the multichannel, radial wavefunctions, and $\mathbf{O}$ and $\mathbf{H}_0$ are the same overlap and field-free Hamiltonians described in previous sections. The form of $\mathbf{F}_E$ is the same as found in Eq. (2.2) where there are two linearly independent solutions for each electronic channel. These solutions are calculated within a finite internuclear volume and do not have the proper normalization nor phases required for the analysis. The scattering states are obtained by matching the numerical solution to an asymptotic form of the wavefunction at some internuclear distance R_0. This distance must be large enough that the numerical solution has reached the known asymptotic behavior. The required form of the functions depends on the long-range behavior of the potentials.

Since we are solving a second-order differential equation, the asymptotic solutions in each dissociation channel can be written down, in general, as a linear combination of regular, f_i, and irregular, g_i, solutions for a given electronic channel, i. These analytical solutions take the form of energy-normalized, standing-wave solutions for the wavefunction at $R = \infty$. The scattering matrix, $\mathbf{S}$, can then be constructed as

$$\mathbf{S} = \left(\mathbf{I} - i\mathbf{J}\right)^{-1} \left(\mathbf{I} + i\mathbf{J}\right), \tag{2.10}$$

where the elements of $\mathbf{I}$ and $\mathbf{J}$ are

$$I_{ij} = \left.\frac{W(g_i, F_{E,ij})}{W(g_i, f_i)}\right|_{R_0}, \tag{2.11}$$

and

$$J_{ij} = \left.\frac{W(f_i, F_{E,ij})}{W(g_i, f_i)}\right|_{R_0}. \tag{2.12}$$

Here, $W(\alpha, \beta)$ is the Wronskian that is defined by the following,

$$W(\alpha, \beta) = \alpha\beta' - \alpha'\beta. \tag{2.13}$$

For the work presented in this thesis, we construct the scattering states we require for our energy analysis. This scattering of the nuclei during dissociation is a half collision, where the nuclei are close together before scattering. We begin with the equation

$$\mathbf{F}_E^{(-)} = \mathbf{F}_E(R_0)\mathbf{A} = \mathbf{f}^{(-)}\mathbf{S}^\dagger - \mathbf{f}^{(+)}, \tag{2.14}$$

where $\mathbf{F}_E^{(-)}$ represents the *physical* solution we desire for our analysis—energy-normalized solutions outgoing on only one channel, and $\mathbf{f}^{(-)}$ and $\mathbf{f}^{(+)}$ are diagonal matrices that describe energy normalized solutions that are incoming $(-)$ or outgoing $(+)$ on a single electronic channel with momentum k_i. For example, the solutions used for HD^+ take the following form,

$$f_i^{(\pm)} \longrightarrow \sqrt{\frac{\mu}{2\pi k_i}} e^{\pm i k_i R}. \tag{2.15}$$

After solving Eq. (2.14) for $\mathbf{A}$, we can express the final scattering solution as the matrix-matrix product

$$\mathbf{F}_E^{(-)}(R) = \mathbf{F}_E(R)\mathbf{A}. \tag{2.16}$$

With this, the observables described in the previous section can now be computed.

2.5 Convergence

In numerical calculations, we have uncertainty caused by grid density, time step, and other parameters. The degree of convergence of our observables tells us how many digits are free of this numerical uncertainty. Specific details of the convergence will be discussed in following chapters. Here, we will discuss the general strategy used for all cases.

We are concerned with the convergence of the energy distribution described by Eq. (2.7). Any integrated quantities, such as branching ratios, will have the same, or better, degree of convergence. The following are the parameters that determine the confidence we have in the numerical calculation;

- Box size — R_{min} and R_{max}
- Density of points in R
- Integration time — t_{min} and t_{max}
- Time step
- Error tolerance of the Lanzcos propagation

The level of convergence is found by changing one parameter, such as increasing R_{max}, while keeping all others fixed until the observable remains constant for as many digits as desired. This process is repeated for all other parameters such that we find convergence in all of our parameter space. In the work presented in this thesis, the degree of convergence is determined by looking at the largest few orders of magnitude of the energy distribution as a function of these convergence parameters. The required values of these parameters are sensitive to both the system we study as well as the properties of the laser pulses. Therefore, convergence testing is required before starting any new calculation even if no changes to the code are made.

Chapter 3

Role of the Permanent Dipole Moment in Strong-Field Dissociation of HD^+

3.1 Introduction

The hydrogen molecular ion, H_2^+, has proven to be an invaluable system to study molecular dynamics [16, 17], but it lacks some important properties that exist in more complex molecules. While similar in many ways, HD^+ differs in a few major respects that make it a compelling system to study. Perhaps the most notable difference is that there are now chemically distinguishable dissociation channels. This allows for the exploration of control over the branching ratios of the dissociating fragments in a relatively simple system [18, 19]. In addition, the potentials have avoided crossings in the lowest two electronic states with nonadiabatic coupling between the electronic and nuclear degrees of freedom—allowing for nonradiative transitions to occur between electronic states. This coupling increases the available pathways the molecule can take while dissociating. The number of these path-

ways are further increased, when compared to H_2^+, if the permanent dipole moment (PDM), originating from the difference between the center of mass and the center of charge, is also taken into account.

Particular interest has been directed at exploring the role of the PDM and how it alters the expectations from the well-studied H_2^+. A theoretical study by Levesque *et al.* [20] examined spatial dependence of their dissociation yields. Using a semi-static picture for the electric potential in a field, they show that the PDM gives an orientation-dependent modification of the potentials. This modification leads to a favored direction for the molecule to dissociate to a given final product. Kondorskiy *et al.* [21] performed a calculation with an 800 nm pulse where they saw additional structures appear in their kinetic energy release (KER) spectrum when they include the permanent dipole terms. Charron and coworkers [18] performed calculations for two-color pulses with central wavelengths of 5.6 and 10.2 μm. They achieve greater control over their observables by controlling the interference between pathways originating from permanent dipole transitions and those coming from electronic transitions. McKenna *et al.* [22] performed kinematically complete measurements of the dissociation of HD^+ with 800-nm pulses to reproduce the results reported by Kiess *et al.* [23] who showed evidence of permanent dipole transitions. McKenna and co-workers found no explicit evidence of permanent dipole transitions and that the result reported by Kiess *et al* was a byproduct of not measuring the dissociating fragments in coincidence. Bhattacharya and Bhattacharya [24] explored the role of the nonadiabatic coupling (NAC) and permanent dipole transitions with intense, 800-nm pulses. They found that the branching ratios' dependence on the NAC and PDM varied greatly with pulse length and intensity.

In this chapter, we present a study of HD^+ in wavelength regimes that have mostly been unexplored. We take advantage of our numerical calculation to explicitly determine the role of permanent dipole transitions by performing the calculations including or neglecting the PDM. We identify where the PDM is important and explore when and how it influences our

observables.

3.2 Matrix Elements of HD^+

The calculation of the field-free Hamiltonian and dipole matrix elements required to solve the TDSE has been outlined in detail in [6]. Here, we will provide a short description of the essential details that pertain to this chapter. The common implimentation of the BO approximation, where the nuclear masses are chosen to be infinite in the electronic Hamiltonian, does not distinguish between HD^+ and H_2^+ — incorrectly leading to degenerate thresholds for HD^+. Solving the system at the geometric center introduces a symmetry breaking term, $-1/2\mu_\alpha \bigtriangledown_R \cdot \bigtriangledown_r$, that couples the electronic and nuclear degrees of freedom and is typically neglected. A common approach to separate the thresholds is to use a unitary transformation to move the symmetry breaking term from the kintetic energy operator to the potential energy operator [18, 24]. This results in a mixture of the *gerade* and *ungerade* symmetries of H_2^+ obtained by the standard BO picture and gives new adiabatic potentials that have separated, but not exact, thresholds and create avoided crossings where non-adiabatic transitions can occur. In our approach, we solve the system in the center of mass frame where this symmetry breaking term does not appear. In addition, we obtain the exact thresholds by including nuclear kinetic energy components in the electronic Hamiltonian [6]. The lowest two electronic channels, $1s\sigma$ and $2p\sigma$, that we use in our calculation are shown in Fig. 3.1.

The form of the electric field used in the laser-molecule interaction described by Eq. (2.4) is

$$\mathcal{E}(t) = \mathcal{E}_0\, e^{-\left(\frac{t^2}{\tau^2}\right)} \cos(\omega t). \tag{3.1}$$

Here, ω is the central laser frequency, and $\tau = \sqrt{2\ln 2}\,\tau_{\text{FWHM}}$ with τ_{FWHM} the intensity full-width-half-max (FWHM) pulse duration. The intensity and τ_{FWHM} used for all wavelengths

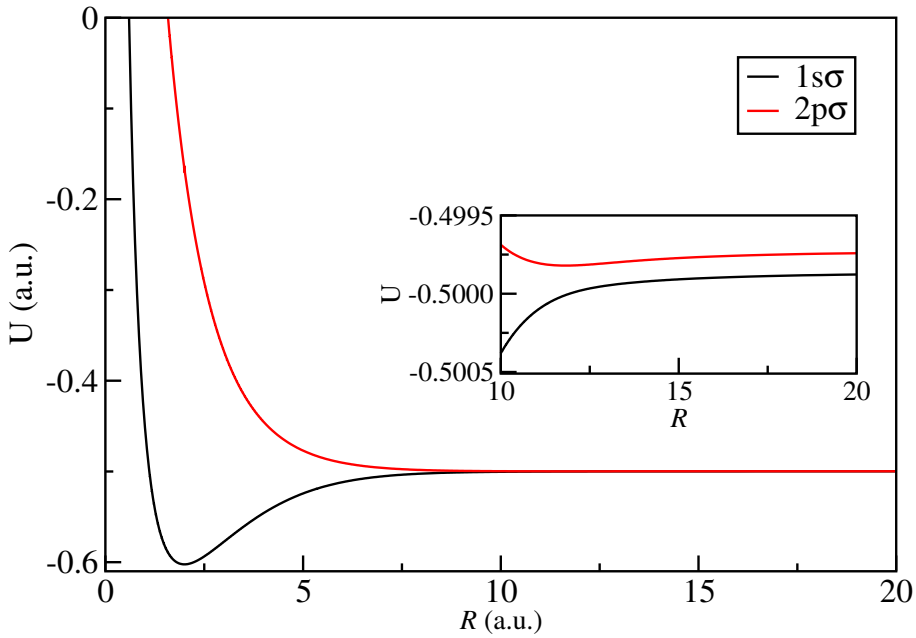

Figure 3.1: *$1s\sigma$ and $2p\sigma$ potential energy curves. The separation of the two channels can be seen in the inset.*

are 10^{13} W/cm^2 and 65 fs, respectively. The pulse length was chosen such that there was a minimum of 5 cycles in τ_{FWHM} of all laser pulses so that we can ignore carrier-envelope phase (CEP) effects [25] and set the CEP to zero for all calculations presented here. Since we are studying the dependence of the system on a single laser parameter, it is important to keep as many parameters constant as possible to avoid introducing unintended effects. By fixing the intensity and pulse duration, the only possible effects we see can be attributed to the changing wavelength.

The nonadiabatic coupling and dipole matrix elements [6], seen in Eq. (2.3), are shown in Figs. 3.2 and 3.3, respectively. The location of the avoided crossing is clearly seen in the sharp peak of the **P**-matrix elements at around $R \sim 12$ atomic units. At around the same internuclear distance, the transition dipole matrix element begins to exponentially decrease towards zero. A physical interpretation of this decrease is that it is the point where the electron has to "decide" which nucleus it will end up on as the molecule dissociates. The permanent dipole elements are small compared to the transition matrix elements at small

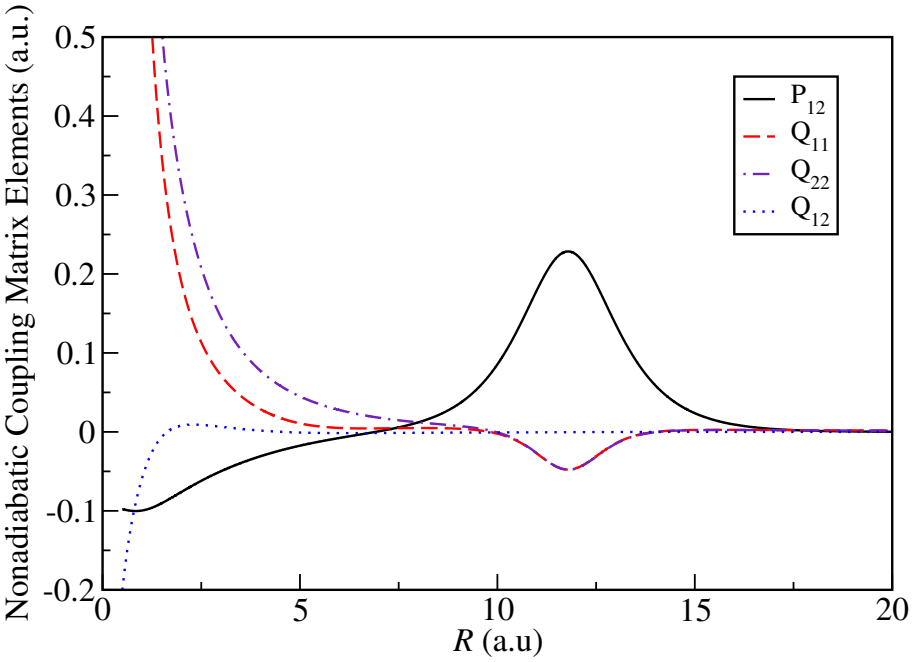

Figure 3.2: *Nonadiabatic coupling matrix elements* **P** *and* **Q** *as a function of* R.

R, but approach their classical values of $\frac{2}{3}R$ and $-\frac{1}{3}R$ as $R \to \infty$.

3.3 Convergence

For the results presented in this chapter, we obtain a minimum convergence of 4 digits for the branching ratios and the main features in the energy spectrum. This required about 9500 non-uniform radial grid points in a box ranging from 0.5 to 400 atomic units. The required box size and number of grid points can be reduced considerably if one only wishes to achieve this level of convergence for the branching ratios or only wishes to examine initial states that have a large dissociation probability. The time step used was 0.125 a.u. with $t_{\min}$ and $t_{\max}$ corresponding times where the intensity of the pulse was 10^4 W/cm^2 and 10^{-4} W/cm^2, respectively. The value of $t_{\max}$ and maximum box size can be reduced by nearly an order of magnitude if one does not calculate the final channel probabilities in the TDSE calculation.

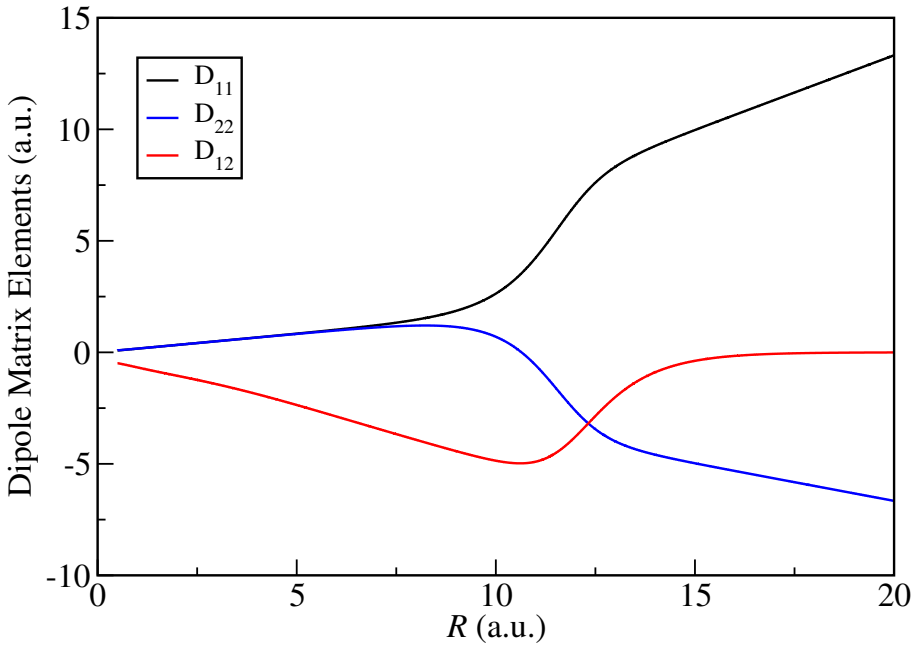

Figure 3.3: *Permanent and electronic dipole matrix elements as a function of R.*

3.4 Permanent Dipole Dependence of Observables

We start our analysis by looking at the total dissociation probability of the fragments as a function of laser wavelength. This will provide a relatively simple look at how the PDM influences the dissociation process. The probabilities are plotted in Figs. 3.4(a)–(c) for three initial vibrational states of HD^+. The black lines indicate the probability to dissociate with the PDM included while the red lines are the same quantity with the PDM neglected. These and all other values presented in this chapter have been averaged over both orientations of the molecule as discussed previously in chapter 2. The nearly complete overlap of the two lines in the figure show that the PDM has little impact on the total dissociation probability for a broad range of wavelengths. Since total yields do little to inform us about physical processes, more information is required to draw any significant conclusions from this data.

In Figs. 3.5(a)–(c) we examine the branching ratio to the lower dissociation channel, $D(1s) + H^+$, in the same manner as Fig. 3.4. Here, we find that the inclusion of PDM

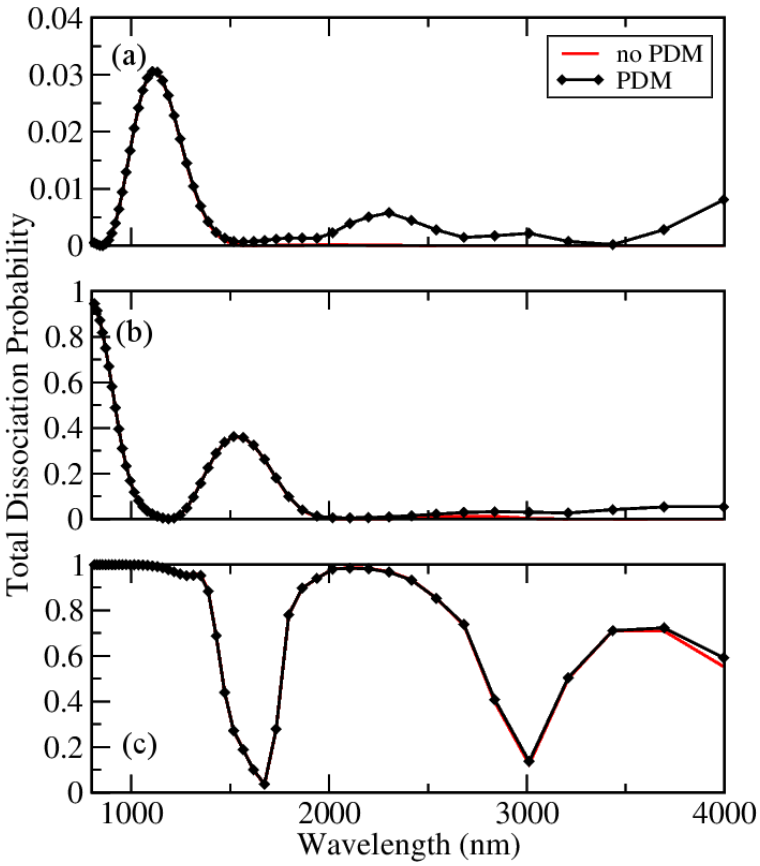

Figure 3.4: *Total dissociation probability as a function of wavelength with the PDM included (black) and without (red) starting from $v = 6$ (a), 8 (b), 10 (c).*

has a considerable impact on the branching ratios even as the total dissociation probability remains largely unchanged. While the physical mechanism cannot be identified by this data, it is clearly seen that the PDM acts as an "equalizer" of sorts where the change in branching ratios are minimized. This effect is similar to the results described in Ref. [24] for HD^+ in the ground vibrational state exposed to a 800 nm, 75 fs pulse at a peak intensity of 5×10^{14} W/cm^2. However, we expect significant ionization to occur at these pulse parameters [7] which is far outside of the approximations used in their study.

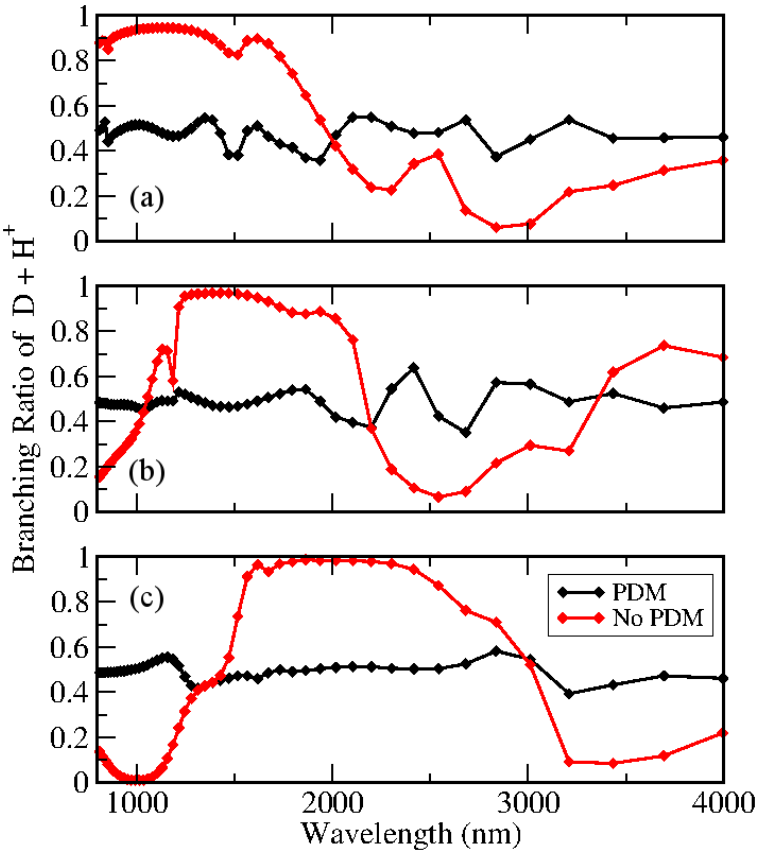

Figure 3.5: *Branching ratio of the D(1s) + H^+ dissociation channel with PDM included (black lines) and without (red lines) as a function of laser wavelength starting from v = 6 (a), 8 (b), and 10 (c).*

3.5 Determining the Role of the Permanent Dipole Moment

Since the PDM cannot directly drive transitions between electronic channels, it must do so in some indirect way in order to have the PDM alter the branching ratios seen in Fig. 3.5. In Figs. 3.6(a)–(c) we plot the energy spectra of dissociating fragments for laser pulses with a central frequency of 0.057 a.u. (800 nm) where the total dissociation probability was found to be unchanged by the PDM, but the branching ratios are heavily affected. Higher-order peaks, indicative of above threshold dissociation (ATD), are not shown in

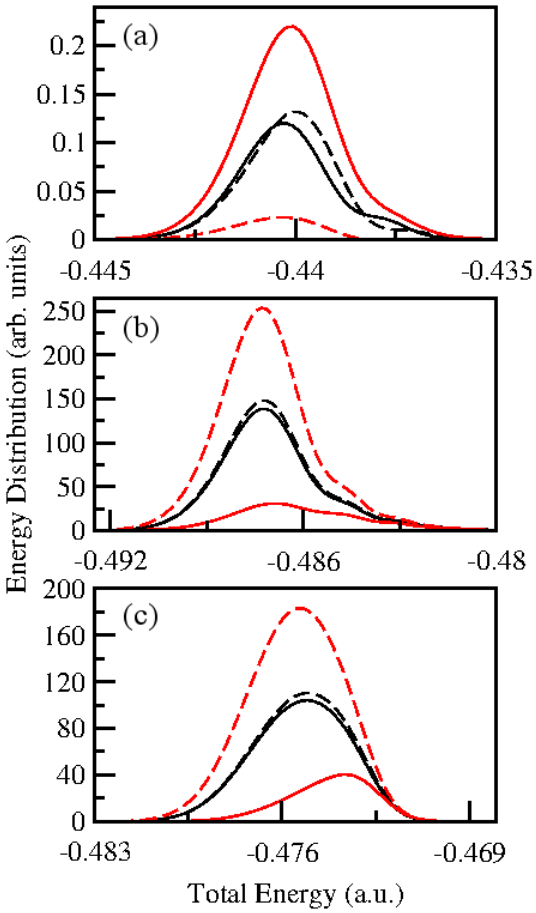

Figure 3.6: *Energy spectra of dissociation to the D(1s) + H^+ channel with PDM included (solid, black lines) and without (dashed, black lines) and to the H(1s) + D^+ with PDM included (solid, red lines) and without (dashed, red lines) starting from v = 6 (a), 8 (b), and 10 (c) with a wavelength of 800 nm.*

these plots since they are smaller than the main peak by at least one order of magnitude. One possible explanation for the the drastic change in the branching ratios with the PDM is that the absorption of one or more photons via the PDM can change the kinetic energy of a dissociating wave packet and influence how the energy-dependent mixing of the dissociation channels occurs via the nonadiabatic coupling. However, this is unlikely because this would require a large amount of ATD which, as previously mentioned, is not the case.

The influence of the PDM on the individual channels is readily apparent in Fig. 3.6, but the energy distribution stays within the same energy range. This suggests that the

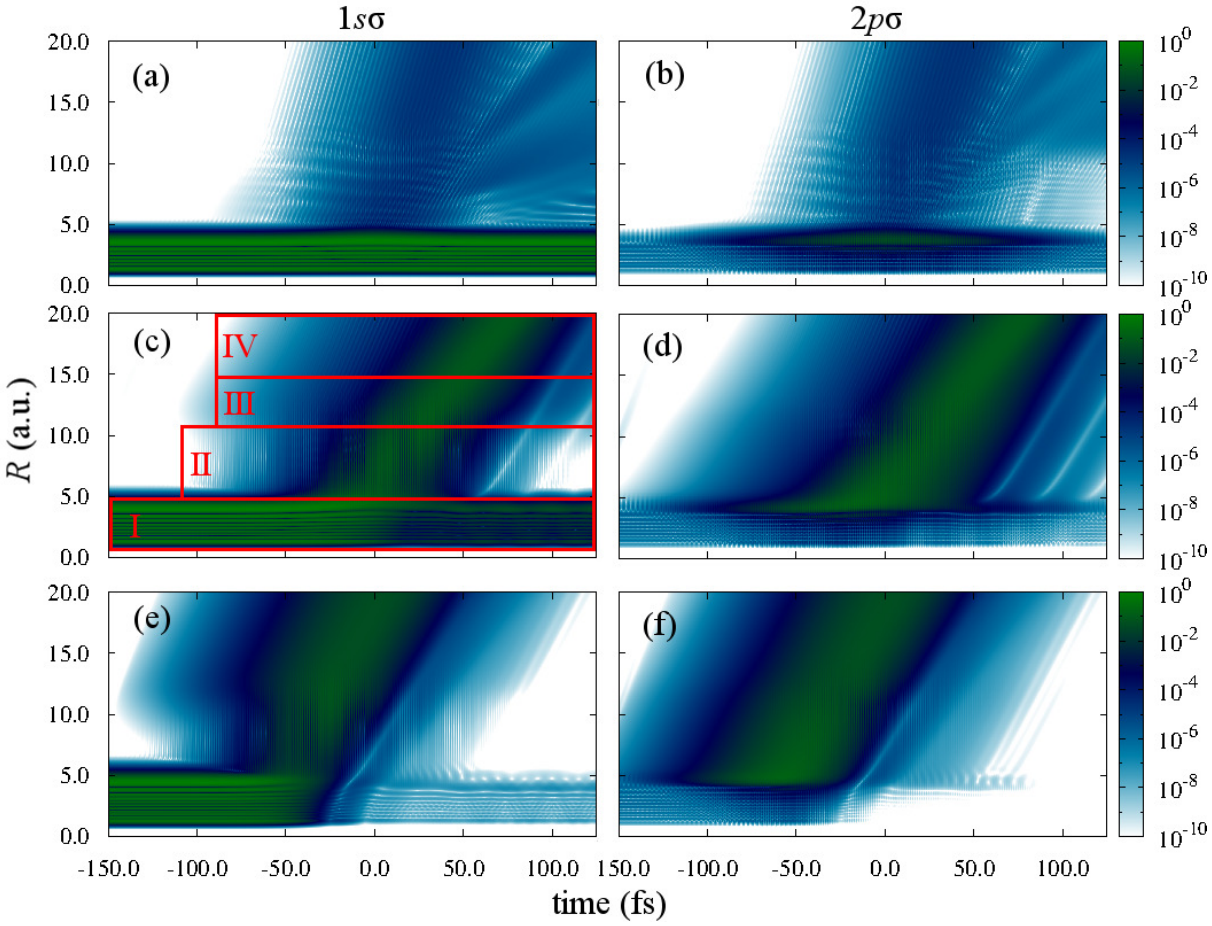

Figure 3.7: *The probability densities of the wavefunction on* $1s\sigma$ *(left column) and* $2p\sigma$ *(right column) as a function of* R *and time starting from* $v = 6$ *(a),(b), 8 (c),(d), and 10 (e),(f) with a laser wavelength of 800 nm.*

introduction of the PDM does not lead to higher net-photon processes, but instead creates new dissociation pathways that lead to the same energy that can then interfere, causing this dramatic change in branching ratios. An example of such a pathway would be a Raman-like transition in the continuum of either $1s\sigma$ or $2p\sigma$ that ends with zero net photons absorbed by the dissociating wave packet.

The probability density as a function of time can be used to see exactly where and when the PDM begins to come into play. The density of the wavefunction on both electronic channels with the PDM included is plotted in Fig. 3.7(a)–(f) for the same parameters used

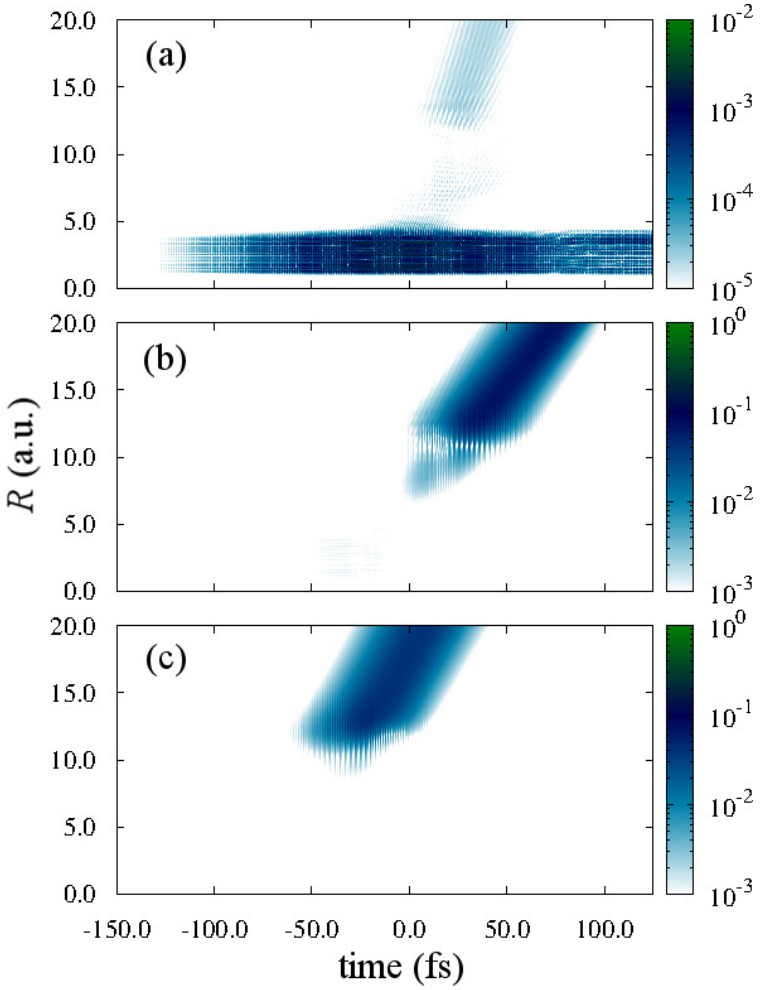

Figure 3.8: *The magnitude of the difference in the probability densities of the wavefunction in the $1s\sigma$ channel with and without the PDM included as a function of R and time starting from $v = 6$ (a), 8 (b), and 10 (c) with a laser wavelength of 800 nm.*

for Fig. 3.6. The main features of these plots can be broken down into four regions which are labeled in Fig. 3.7(c) as well as a simple schematic shown in Fig. 3.9. In region I, we see the bound part of the wavefunction on the $1s\sigma$ channel as well as excitation to $2p\sigma$. For the leading and trailing edges of the pulse, we see vertical stripes present on both electronic channels but do no dissociation. This is indicative of the field driving Rabi-like transitions between the two electronic channels. These transitions continue to occur to the dissociating wave packet located in region II. A significant change occurs in region III where

the magnitude of the probability density in both channels changes rapidly over a small range of R. Since this is the location where the NAC, EDM, and PDM are all at their largest, it is difficult to determine what mechanism(s) cause this sudden shift in the density. By the time the wave packet reaches region IV, the NAC and EDM have become negligible and the evolution of the wave packet resembles field-free propagation.

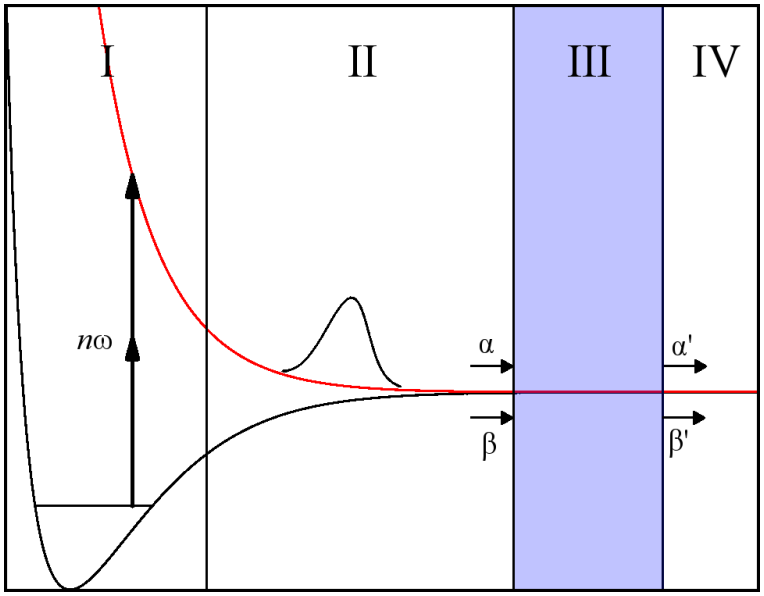

Figure 3.9: *Schematic for the dissociation dynamics.*

In order to more explicitly determine the role of the PDM, the magnitude of the difference of the probability density on $1s\sigma$ with and without the inclusion of the PDM are shown in Fig. 3.8. The most notable feature of these plots that we observe is that the difference is very small in region II. This means that permanent dipole transitions play no role in the creation of the dissociating wave packet. This is true even when there is clear vibrational excitation, as demonstrated for $v = 6$ in Fig. 3.8(a). The vertical stripes seen in Fig. 3.7 can also be seen in region III of the difference, meaning that the PDM is responsible for altering the frequency of the wave packet that is transfered between the two channels.

From Fig. 3.8, we learned that the PDM's effect on the branching ratios occurred at values of R around the avoided crossing (region III in Fig. 3.9). In this region, the NAC,

EDM, and PDM are all relatively large, so it is unclear exactly what mechanism(s) play the most dominant role in the dynamics we observe. In order to discern the relevant mechanisms, we performed a few tests of the interactions between the NAC, EDM, and PDM by systematically turning these mechanisms "on" or "off" and seeing how the branching ratios changed. We began by testing the importance of the NAC by performing calculations for a few wavelengths including those used in Fig. 3.8 with all combinations of the PDM and NAC being turned on or off. In most cases, the NAC was found to have a nontrivial impact on the branching ratios, but the PDM had larger influence in all cases. To test the importance of the EDM inside region III, calculations were performed using an EDM that was truncated such that it smoothly went to zero before entering the crossing region. The different combinations of the PDM and NAC being turned on or off were tested with this truncated EDM for the 800 nm pulse case in Fig. 3.6. In these cases, the NAC was found to influence the branching ratios more than the PDM which is contrary to the results of the previous test. The result from these studies was that the interactions between the NAC, EDM, and PDM are complex and these tests are insufficient to describe the dynamics in any general way. A more sophisticated approach is necessary to have any hope of unraveling the physical processes at play.

An attempt to explain this phenomena was to solve a two level system that included the full dipole and nonadiabatic coupling matrix elements for a given value of R. In the rotating wave approximation [5], these solutions would be analytical and would explicitly show the relationship between the PDM, EDM, and NAC. The first problem encountered with this approach was that the intensity of the laser we used for the original calculation, 10^{13} W/cm^2, was too large for the rotating wave approximation to apply — meaning that a purely numerical calculation is required. This numerical calculation for the two-level system was carried out, but failed to reproduce the frequency of oscillation of the wave function nor did it given the correct value of the branching ratios. This implies that the radial

dependence of the dipole and nonadiabatic coupling matrix elements must be accounted for in any model we create. However, the failure of the rotating wave approximation means that following this line of modeling will not lead us to a simple, analytical expression for the physics we wish to describe.

A logical next step in this study would be to perform our calculations including rotation to see if this phenomena persists in order to ensure that what we observe is not a mere byproduct of neglecting nuclear rotation. Alternatively, or in addition to this, the radial wavefunction could be decomposed into different, net-photon components via a Fourier transform with the carrier-envelope phase of the laser pulse. This would allow us to see exactly when and where photons were being absorbed or emitted as the dissociating wave packet travels outward and through the avoided crossing. While we still would not have an elegant, analytical solution, we could have a much clearer picture of the dissociation dynamics without the need to model our system. Clearly, more work needs to be done in exploring the options available and determining the most appropriate route that gives us the most relevant information.

Chapter 4

Carrier-Envelope Phase Control Over the Branching Ratios in Strong-Field Dissociation of HD^+

4.1 Introduction

Controlling the final products of a chemical reaction using a strong-field laser has long been a goal of ultrafast science. The ability to generate intense, few-cycle pulses made the carrier-envelope phase (CEP) — the phase difference between the envelope and carrier — an important control knob of the laser field to explore. Much experimental and theoretical work has been focused on investigating CEP control over the direction of charged fragments after photodissociation or dissociative ionization for simple molecules such as H_2^+ [26, 27, 28, 29] and D_2^+ [30] or over the direction of the ejected electron from atomic and molecular systems [31, 32]. Surprisingly, less focus has been directed at achieving CEP control over yields and branching ratios [33, 34] — which is, arguably, a more interesting and desirable observable to control.

A general, photon-based theory has been developed [25] that gives insight into what physical processes must be involved to have CEP dependence in a given observable. From these works, we learn that CEP dependence of a yield is, in general, more difficult to obtain as it requires interferences between higher-order processes in comparison to what is needed for spatial asymmetry. Barring a few exceptions [35, 36, 37, 38, 39], previous work used laser fields with a central wavelength between 700 nm and 800 nm. For these wavelengths, dissociation of H_2^+ and D_2^+ is typically dominated by 1–2 net-photon processes—meaning the CEP control over yields is not expected to be large. It is then not too surprising that controlling the dissociation yields has not become a hot topic in ultrafast physics.

With greater advances in the creation of intense, few-cycle pulses at longer wavelengths [40, 41], the ability to control yields warrants more examination. For pulses longer than the typical 800 nm, the number of photons exchanged with the field is expected to be larger—giving a greater chance to control the yields via the CEP. We present a theoretical study of strong-field dissociation of HD^+ for few-cycle pulses with wavelengths ranging from 800 nm to 4000 nm. The CEP dependence of the energy spectra, total yields and branching ratios are calculated for these laser parameters. We analyze these observables using the photon-phase formalism that was established in Ref. [25] and use it to determine what pathways give us the most control using the CEP and explore their wavelength dependence.

4.2 Photon-Phase Formalism

An exact theory that defines how the CEP affects molecular systems has been previously developed [25, 33]. The result is that the CEP control comes from the interference of processes that differ by some specific values of net-photons exchanged with the field. For example, the CEP dependence of the total yield for a single-color laser pulse comes from net-photon processes that differ by an even number of photons. This simple result depends largely on

total parity dictating what terms survive and eventually lead to the CEP dependence seen in the observables. Total parity is usually accounted by keeping track of the total angular momentum J. A problem can arise when applying this theory to calculations where the nuclear rotation is not included. For such cases, it is common to have the internuclear distance to be only positive-valued which limits the space the nuclei can occupy. This means that there are no parity eigenstates for this system. In the previous case of H_2^+ in 1-D [33], the parity of the electronic states was sufficient to give the expected CEP dependence given by a full 3-D calculation. If this same treatment was applied to a heteronuclear molecule, it would fail to recover the correct CEP dependence since there is no *gerade* and *ungerade* symmetry. The goal in the following derivation is to connect our calculations for HD^+ without parity eigenstates to those that have parity eigenstates explicitly included.

We will begin with describing the formulation that has eigenstates of total parity for each electronic state. In the two-channel approximation, the total wavefunction can be written down as

$$\mathbf{\Psi} = \begin{pmatrix} F^e_{1s\sigma} \\ F^e_{2p\sigma} \end{pmatrix} |e\rangle + \begin{pmatrix} F^o_{1s\sigma} \\ F^o_{2p\sigma} \end{pmatrix} |o\rangle, \tag{4.1}$$

where e and o denote even and odd total parity, respectively. Since these are eigenstates of total parity, they have the following relation,

$$\Pi F_i^{e,o}|e,o\rangle = \pm F_i^{e,o}|e,o\rangle, \tag{4.2}$$

where Π is the parity operator and i is the channel index.

Since our calculation is for a molecule with a fixed orientation, we want to recast Eq. (4.1) as a sum of wavefunctions corresponding to the two possible orientations of the molecule.

This is done by using the transformation,

$$|e\rangle = \frac{1}{\sqrt{2}}\big(|R\rangle + |L\rangle\big) \tag{4.3}$$

and

$$|o\rangle = \frac{1}{\sqrt{2}}\big(|R\rangle - |L\rangle\big), \tag{4.4}$$

where $|R\rangle$ and $|L\rangle$ denote the orientation of the nuclei. Here, we note the scattering states discussed in Ch. 2 are not eigenstates of total parity since they must describe a state dissociating in a particular direction.

Applying equations (4.3) and (4.4) to Eq. (4.1) and projecting onto scattering states gives the following expression for the differential dissociation probability in terms of single-orientation wavefunctions:

$$\frac{dP_i}{dE} = \left[\left|\left\langle F^{\mathrm{R}}_{i,k_i}|F^{\mathrm{R}}_i\right\rangle\right|^2 + \left|\left\langle F^{\mathrm{L}}_{i,k_i}|F^{\mathrm{L}}_i\right\rangle\right|^2\right]. \tag{4.5}$$

Here, i is the channel index and k_i is the momentum. This expression assumes that the molecule starts in an even parity eigenstate. However, since the molecule is not allowed to change orientations in our calculation, the initial state does not have even parity. This introduces an extra normalization factor that must be accounted for in the wavefunctions obtained in our calculation. This means that we take an orientation average of our observables instead of the sum over both orientations described by Eq. (4.5). With this step, we are able to connect our calculations to those calculated using eigenstates of total parity.

The electric field we consider has the form

$$\mathcal{E}(t) = \mathcal{E}_0(t)\cos(\omega t + \varphi), \tag{4.6}$$

where φ is the CEP. From Refs. [25, 33], we learn that since the field is periodic in φ, the Hamiltonian and wavefunction must also be periodic in φ. This means that the time-dependent wavefunction can be expanded in a Fourier series where the φ dependence is given explicitly:

$$\mathbf{F}^{\mathrm{R,L}}(R,t) = \sum_n \mathbf{F}_n^{\mathrm{R,L}}(R,t)e^{in\varphi}. \tag{4.7}$$

Here, n is the net number of photons absorbed of frequency ω. Since the overall change in sign needed to change the orientation can be represented as a shift in the CEP, $\varphi \to \varphi + \pi$, the values of $\mathbf{F}_n^{\mathrm{R}}(R,t)$ and $\mathbf{F}_n^{\mathrm{L}}(R,t)$ must be identical. In addition, from Ch. 2 we know that the orientation can be switched by changing the overall sign of the laser-molecule interaction term. This means that the scattering states, F_{i,k_i}^{R} and F_{i,k_i}^{L}, are identical because they are calculated independent of the field.

After combining and simplifying Eqs. (4.7) and (4.5), we obtain the following expression:

$$\frac{dP_i}{dE} = \frac{1}{2}\sum_{n,n'}\left[\langle F_{i,k_i}|F_{i,n}\rangle \langle F_{i,k_i}|F_{i,n'}\rangle^* e^{i(n-n')\varphi}\left(1+e^{i(n-n')\pi}\right)\right]. \tag{4.8}$$

In agreement with Ref. [33], we find that for any CEP dependence in the differential dissociation probability and, by extension, any yields, the quantity $n-n'$ must be an even number. Here, we note that the CEP dependence without performing an orientation average means that no restriction of the allowed values of $n-n'$ can be made thus giving the incorrect CEP dependence in the observables.

We now have an exact form for the CEP dependence of observables that comes from interference between two pathways that originate from the absorption of a different number of photons. Using this formalism, we can rewrite the observables as a Fourier series:

$$P = \sum_{k \text{ even}} P_k \cos(k\varphi + \delta_k). \tag{4.9}$$

Here, P can be the differential dissociation probability, channel or total yields, and branching ratios, while k is the value of $n - n'$ in Eq. (4.8), P_k is the magnitude of the CEP-oscillation with frequency k, and δ_k is a k-dependent phase. The relative magnitudes of P_k can tell us what photon processes are most important to explain the CEP dependence of our observables. This will be discussed in more detail in the following sections where we use Fourier transforms of the observables to explicitly define their dependence on CEP.

4.3 Numerical Details

The method used to solve the TDSE and the matrix elements used are exactly the same as described in Chapters 2 and 3. The only difference is the intensity of the electric field used. The most notable difference is that the CEP of the pulse is no longer fixed to zero, and is now a control knob for our calculation. While the parameters of the field have changed, the requirements for and the degree of convergence are exactly the same as described in Ch. 3. This was tested by looking at the energy spectrum from initial states $v = 0, 3, 10,$ and 16 for wavelengths of 800 nm and 4000 nm. Since the degree of convergence was found to be the same for both extremes in wavelength, we assume that the convergence is the same for wavelengths in between.

In order to expand our observables in a Fourier series as described by Eq. (4.9), we must meet some minimum requirements for the density of points in the CEP. Since the expansion we wish to perform is a Fourier transform, we can use the Nyquist critical frequency to determine this density of points [42]. The Nyquist critical frequency is

$$f_c \equiv \frac{1}{2\Delta} \tag{4.10}$$

where Δ is the sampling interval. Any continuous function can be represented exactly by a discrete sampling of points if the sampling frequency is at least twice as fast as the fastest

oscillating component. From this, we learn that our points should be evenly spaced and that the number of points we must use is directly related to the highest value of $n - n'$ that we expect to have in our calculation. For the results presented in this chapter, 32 evenly spaced CEP points were used on an interval $[0, 2\pi)$ to get an accurate Fourier transform of the energy spectra and total yields. The number of CEP points required was found by starting with a small number of points and doubling the amount until the Fourier transform of the energy spectra converged.

4.4 Results and Discussion

We present calculations for the dissociation of the HD^+ molecular ion in a strong field with wavelengths ranging from 800 nm to 4000 nm. For all cases shown below, the peak laser intensity was fixed to 5×10^{13} W cm^{-2} with the pulse duration corresponding to two cycles in the FWHM of the Gaussian laser pulse. Fixing the number of cycles as wavelength is varied keeps the relative bandwidth, $\Delta\omega/\omega$, of the pulse fixed. As stated previously, the CEP dependence comes from interference between different net-photon processes when they overlap at the same energy. If the pulse duration is kept fixed while the wavelength is varied, it naturally increases or reduces this overlap in energy. Since this overlap changes with laser bandwidth, keeping the relative bandwidth fixed is a way to reduce these trivial effects so that the changes in CEP dependence on wavelength is from more significant dynamics of the system.

The CEP-dependent branching ratio, described by Eq. (2.8), for dissociation on the $1s\sigma$ electronic channel as a function of laser wavelength is plotted in Fig. 4.1 for five different initial vibrational states. A general trend can be seen that the magnitude of the oscillations with CEP increase with increasing wavelength independent of initial vibrational state. In addition, we see the introduction of higher frequency terms appearing as wavelength is

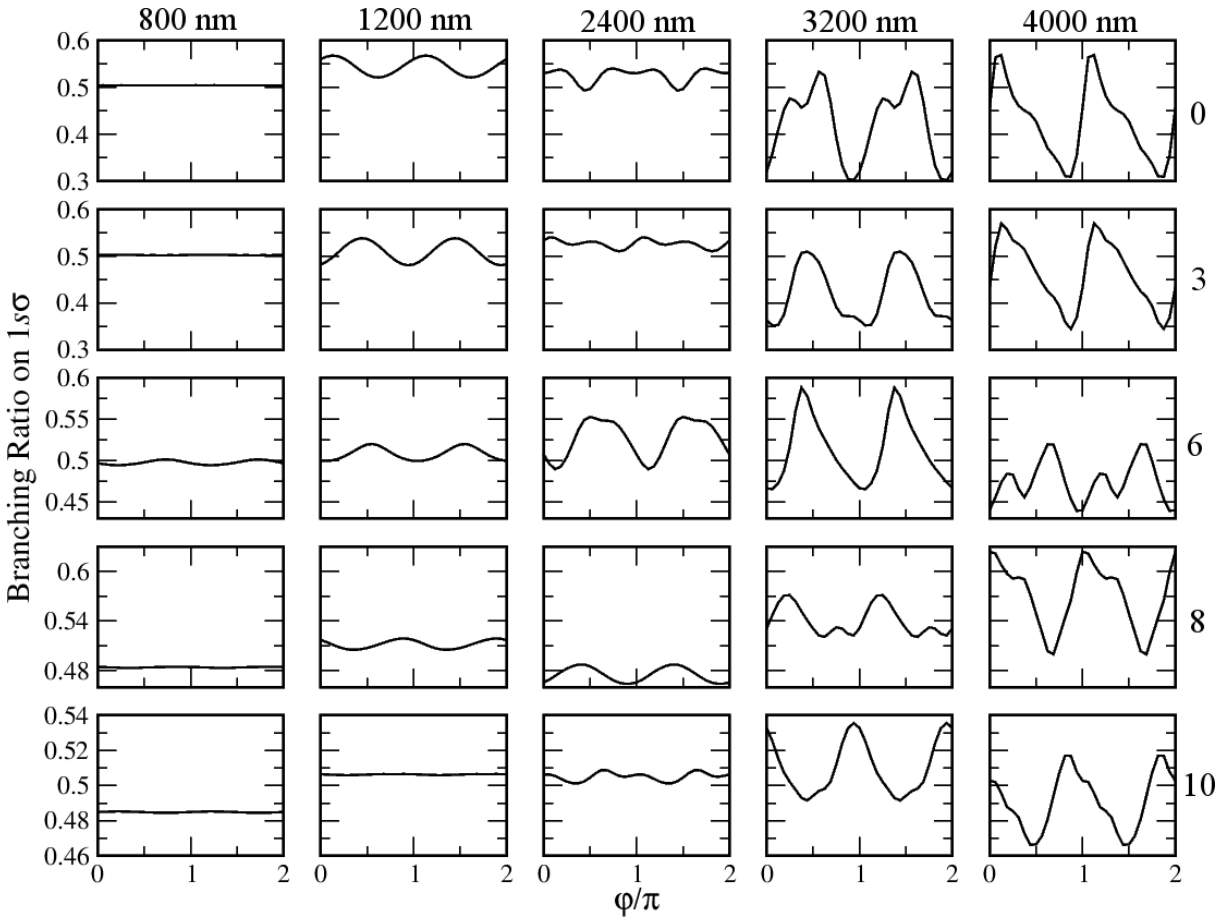

Figure 4.1: *Branching ratio for the dissociation on the* $1s\sigma$ *electronic channel as a function of* φ/π*, where* $0 \leq \varphi/\pi \leq 2$*. Each column corresponds to a wavelength of 800 nm, 1200 nm, 2400 nm, 3200 nm, and 4000 nm. Each row corresponds to an initial vibrational state* $v = 0$*, 3, 6, 8, and 10.*

increased.

The CEP dependence seen in Fig. 4.1 can be quantitatively defined by using the relation in Eq. (4.9) by performing a Fourier transform of the dissociation yield on the $1s\sigma$ channel to obtain the magnitude of the oscillations of a given frequency P_k. The ratios,

$$\mathcal{P}_k = \frac{P_k}{P_0}, \tag{4.11}$$

are plotted in Fig. 4.2 to show how the relative strength of each frequency component changes

with wavelength and initial state. As expected, the magnitude of $\mathcal{P}_k$ quickly becomes small as k is increased since higher-order, net-photon processes need to overlap in energy to produce the higher frequency terms. For example, to see $\cos(6\varphi)$ dependence in the dissociation probability there must be an overlap in energy of different photon-processes differing by 6 net photons absorbed. While we are able to rigorously quantify the CEP dependence, we find no clear trend with the values of $\mathcal{P}_k$ and wavelength. Since the relative bandwidth is fixed, this means that this effect is either due to an increase in pulse energy as wavelength is increased, or that the structure of HD^+ plays an important role in determining what wavelengths are "preferred", or a combination of both.

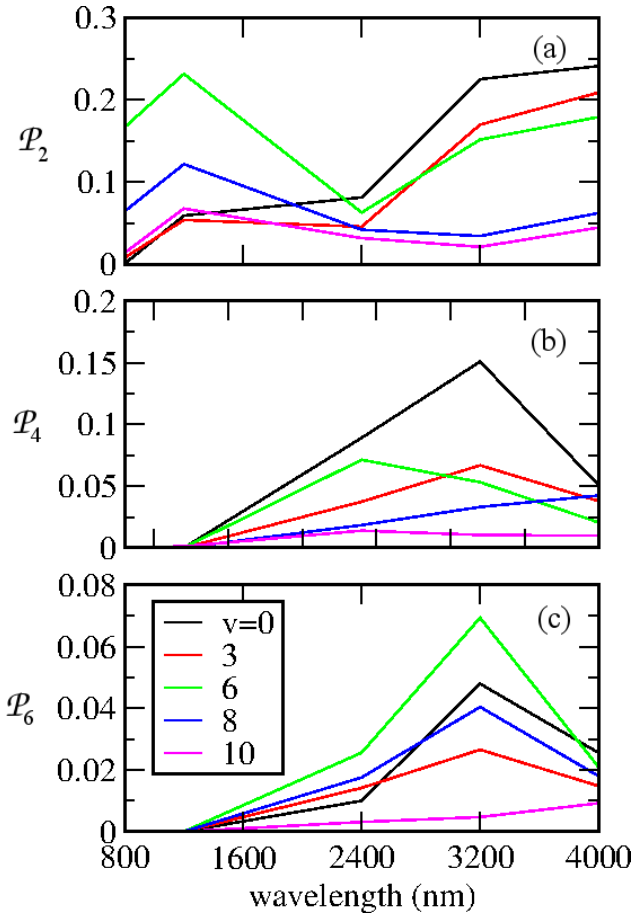

Figure 4.2: *Values of $\mathcal{P}_k$, from Eq. (4.11), obtained by a discrete fourier transform of the data plotted in Fig. 4.1 as a function of wavelength.*

Molecular ions, such as HD^+, are typically produced by ionizing the neutral molecules which means that there is a distribution of initial vibrational states. This distribution can be approximated using the Franck-Condon (FC) principle [5] which assumes that the ionization process occurs instantaneously at a fixed internuclear distance. In this framework, the probability to be in a given vibrational state of the ion is dictated by the overlap of the ground vibrational state of the neutral molecule, v', with the vibrational states of the ion, v, given by

$$f_{v,v'} = |\langle v|v'\rangle|^2. \tag{4.12}$$

The resulting distribution is plotted in Fig. 4.3 where the distribution peaks at $v = 2$ and sharply declines as v increases. In order to account for the effect of the distribution on the final observables, an incoherent sum of said observable over all vibrational states with the appropriate weight is required. Here, we are concerned with the FC average of the dissociation probability outgoing on the $1s\sigma$ channel,

$$P_{1s\sigma} = \sum_v f_{v,v'} P^v_{1s\sigma}. \tag{4.13}$$

Performing a Fourier transform on the result from Eq. 4.13 gives the FC-averaged values of $\mathcal{P}_k$ found in table 4.1. As one may expect, the FC average reduces the magnitude of oscillations with CEP by at least an order of magnitude for all wavelengths. At the same time, the values of $\mathcal{P}_k$ in the 3200 nm case remain on the few-percent level after averaging.

$\mathcal{P}_k$	Wavelength (nm)				
	800	1200	2400	3200	4000
$\mathcal{P}_2$	0.02113	0.03956	0.03853	0.04308	0.02679
$\mathcal{P}_4$	1.307×10^{-4}	1.460×10^{-3}	0.01254	0.02273	8.130×10^{-3}
$\mathcal{P}_6$	7.417×10^{-9}	2.751×10^{-6}	6.151×10^{-3}	0.01564	2.842×10^{-3}

Table 4.1: *Franck-Condon-averaged values of $\mathcal{P}_k$ for dissociation on the $1s\sigma$ channel.*

In order to gain more insight into the dissociation processes involved, we plot the energy

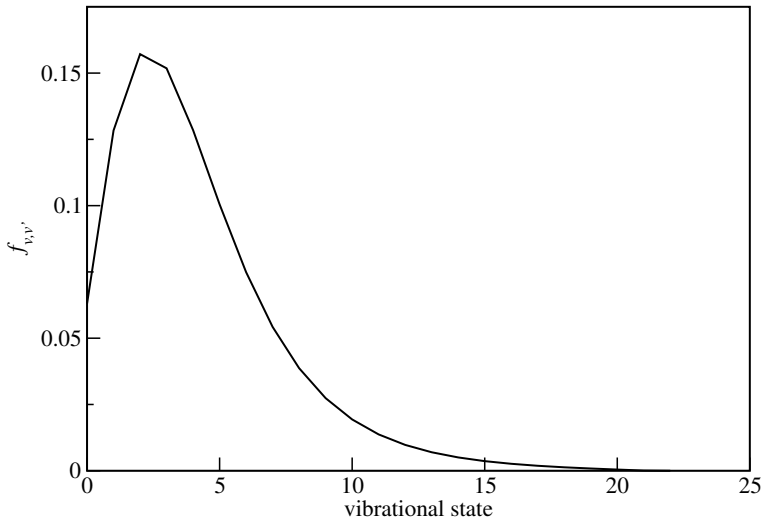

Figure 4.3: *Weight factors, $f_{v,v'}$, as a function of HD^+ vibrational states calculated using the Franck-Condon principle in Eq. (4.12). This forms a Franck-Condon distribution of initial vibrational states.*

distribution of the dissociated fragments for the cases in Fig. 4.1. Since the CEP-dependence of the dissociation probability as wavelength increases is qualitatively independent of initial vibrational state, we choose to study $v = 10$ as an example. The energy distribution for total energies above the $2p\sigma$ threshold are plotted in Fig. 4.4 for five different wavelengths. While the expected π-periodicity in CEP is easily recognized in all plots, it is difficult to isolate any other properties of the distribution. In addition, from the results shown in Fig. 4.2 we should expect to see overlap between processes differing by 6 net photons for a wavelength of 3200 nm (among others), but the energy range at which we see any significant dissociation probability seems to suggest that this is not probable if we use a conservation of energy argument. Three 3200 nm photons are required to dissociate from $v = 10$ which means that nine net photons must be absorbed to produce the $\cos(6\varphi)$ dependence—meaning that the energy distribution is expected to have components going out to at least -10.8 eV in Fig. 4.4. From Fig. 4.4(d), we find that this is clearly not the case. This will be discussed in more detail later in this section.

In order to answer the questions posed by the results in Fig. 4.4, we apply the formulation

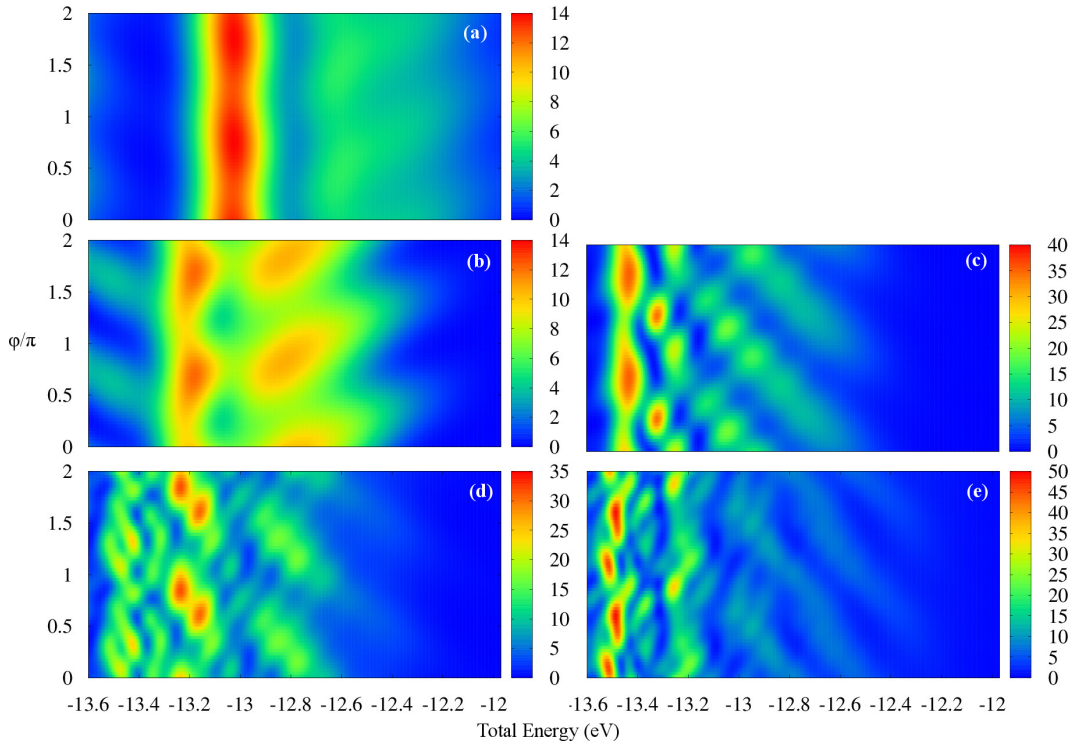

Figure 4.4: *Energy distribution for the dissociation of the* $1s\sigma$ *electronic channel from* $v = 10$ *as a function of CEP for a wavelength of 800 mn (a), 1200 nm (b), 2400 nm (c), 3200 nm (d), and 4000 nm (e).*

described in Eq. 4.9 to describe the, now energy-dependent, magnitude of the oscillations in CEP with frequency k. The relative strength of these components,

$$\mathcal{Y}_k(E) = \frac{dP_k}{dE} \Big/ \frac{dP_0}{dE}, \tag{4.14}$$

are plotted in Fig. 4.5 for the same energy ranges used in Fig. 4.4. The trend with the maximum magnitude of $\mathcal{Y}_k(E)$ and wavelength, where the magnitude grows from 800 nm to 3200 nm and drops off at 4000 nm, is very similar to the trends found in Fig. 4.2. We observe that $\mathcal{Y}_k(E)$ has intricate structures that are dependent on wavelength, but have no clear pattern. This analysis shows that, while the spectrum has a relatively small range in energy, there is a large overlap between many processes that have absorbed many more photons than required to dissociate.

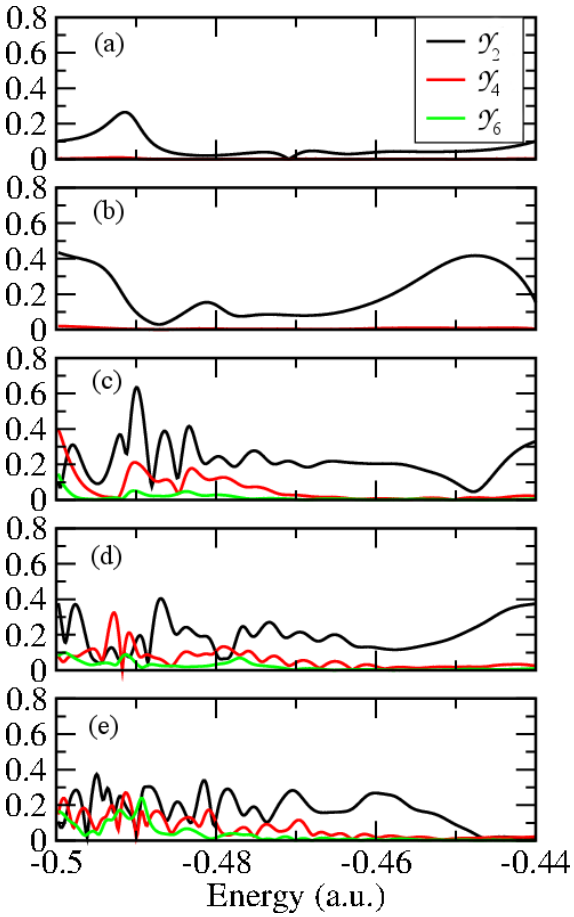

Figure 4.5: *Values of $\mathcal{Y}_k(E)$, from Eq. (4.14), obtained from a discrete Fourier transform of the data plotted in Fig. 4.4 for a wavelength of 800 mn (a), 1200 nm (b), 2400 nm (c), 3200 nm (d), and 4000 nm (e).*

As discussed previously, at least two different processes differing by six photons need to interfere to have any magnitude in $\mathcal{Y}_6(E)$ which seems unlikely from the energy distribution shown in Fig. 4.4. The explanation for this behavior can be interpreted from the expression for the differential dissociation probability described by Eq. (4.8). Here, we see that the amplitude of an n net-photon process is proportional to $\left| \langle F_{i,k_i} | F_{i,n} \rangle \right|^2$, whereas the interference term, that is controlled via the CEP with $\cos(6\varphi)$ dependence, is determined by a term proportional to $\langle F_{i,k_i} | F_{i,n} \rangle \langle F_{i,k_i} | F_{i,n+6} \rangle^*$ and its complex conjugate. Since the interference does not depend on the square of $\langle F_{i,k_i} | F_{i,n} \rangle$, we can expect to see contribution from higher-

order photon processes even though its corresponding "peak" in the energy distribution is very small.

4.5 Summary

In this chapter, the photon-phase formalism was introduced in order to analyze the CEP-dependent dissociation of HD^+ with several different wavelengths. While no clear wavelength dependence for CEP control was obtained, we find that the formalism can be used to extract more information from measured or calculated observables. For instance, it was found that higher-order photon processes were influencing the dissociation probabilities more than the energy distribution would suggest. This is important information for those trying to determine what physical processes led to the observables they find in a given system because it gives a better idea of how many photons were involved in the reaction.

Chapter 5

Strong-Field Control of Dissociation of LiF Using a Pump-Probe Scheme

The alkali-metal-halide (AMH) family of molecules are of particular interest to study with intense, ultrafast lasers. In general, the lowest two electronic states of AMHs, an ionic state and a covalent state, have an avoided crossing—giving rise to nonradiative transitions between them. The Coulomb potential found in the ionic channel introduces an infinity of states that are either bound states or resonant states with the continuum of the covalent channel. The nature of these potentials, in addition to the relatively heavy mass of AMHs, make them ideal for studying dissociation dynamics on a femtosecond time scale. Zewail and co-workers pioneered the field of femtochemistry with their study of the dissociation of NaI [2, 43] and other systems using a pump-probe scheme.

We turn our attention to LiF as a good candidate to control using intense fields. A theoretical study by Bandrauk and Gaunthier [44] looked at strong-field dissociation of LiF using a single laser pulse. They calculate the branching ratio between the ionic (Li^++F^-) and covalent (Li+F) channels with wavelengths between 2 and 10 μm and intensities from 7×10^{12} to 5×10^{14} W/cm^2. They find that 60–90% of the total dissociation yield is in the

covalent channel. A study by Qing-Tian and Varandas [45] numerically explored intensity effects on the dynamics of the dissociating wave packet as well as the energy distribution of the fragments in the covalent channel.

Our goal is to control the branching ratios as for HD^+, but the properties of LiF suggest a different approach than we took with HD^+. We follow in a similar vein of Zewail and co-workers by employing a pump-probe scheme where we take advantage of the relatively heavy mass of the molecule that allows for a clear distinction between the interactions of the molecule with the pump pulse and with the probe pulse since they do not overlap in time. This allows us to have a clear understanding of the physical processes involved during dissociation and use them to achieve considerable coherent control over the branching ratios.

5.1 Potential and Dipole Matrix Elements

In the case of LiF, we solve the TDSE in the same way as described in Ch. 2; however, the electronic potentials and dipole matrix elements are taken from a Multi-Configuration Self-Consistent Field (MCSCF) calculation by Werner and Meyer [1]. The values of the thresholds is an especially important feature to correctly treat for LiF because the energy separation between the ionic and covalent thresholds dictates where the avoided crossing appears. For the calculation in Ref. [1], they choose their configurations such that they obtain the correct energy separation of ~ 2 eV, giving the location of the avoided crossing at $R \sim 13$ atomic units.

Diabatic and adiabatic electronic potentials as well as dipole matrix elements for internuclear distances from 2 to 20 atomic units are provided by Werner and Meyer. In addition, the off-diagonal elements of the first-order radial couplings, $\mathbf{P}$, are provided for a few radial points around the avoided crossing. In order to have structure suitable for a calculation involving dissociation, the diabatic potentials and dipole matrix elements are extrapolated

to both small and large internuclear distances. From theory, the asymptotic form of the covalent channel is described by a van der Waals potential which is proportional to $-R^{-6}$. It is important to note that the value of the covalent potential is already constant down to a magnitude of 10^{-3} for R from 13.4–20 atomic units, meaning that the choice of the asymptotic form of the potential only needs to smoothly reach the known value of the threshold. For this reason, an exponential function was used as it was found to be a better fit for the data provided in Ref. [1]. The ionic channel follows the form of the Rittner potential [46],

$$V_{\text{ionic}}(R) = -\frac{1}{R} - \frac{\alpha_{Li^+} + \alpha_{F^-}}{2R^4} - \frac{\alpha_{\text{fit}}}{R^7}, \tag{5.1}$$

where $\alpha_{Li^+} = 0.193$ a.u. and $\alpha_{F^-} = 13.5$ a.u. are the polarizabilities of Li^+ and F^-, respectively, and α_{fit} is a fit parameter. The form of the potentials used for small R are a modified Morse-like potential,

$$V(R) = \beta_0 e^{-\beta_1(R-R_1)} \left(e^{-\beta_2(R-R_2)} - 1\right), \tag{5.2}$$

where all values except for R are fit parameters that depend on the electronic channel.

In the diabatic picture, the dipole matrix elements have simple behavior that we use for our extrapolation. In the separated atom limit, the permanent dipole moment (PDM) for the ionic channel goes to the classical limit of $D_{\text{ionic}} \to R$ while the PDM for the covalent channel, as well as the electronic dipole moment, goes exponentially to zero. In the unified atom limit, all dipole matrix elements smoothly approach zero as $R \to 0$.

5.2 Matrix Elements in the Adiabatic Representation

Following the formulation in Ref. [1], the wavefunction in the adiabatic representation is related to the diabatic representation by,

$$\mathbf{\Psi}_{\rm ad} = \mathcal{U}^{\dagger}\mathbf{\Psi}_{\rm d}, \tag{5.3}$$

where $\mathcal{U}$ is the matrix that diagonalizes the diabatic potential matrix at a given R. The adiabatic dipole matrix elements are then obtained by the following operation,

$$\mathbf{d}_{\rm ad} = \mathcal{U}\mathbf{d}_{\rm d}\mathcal{U}^{\dagger}. \tag{5.4}$$

The adiabatic potentials and dipole matrix are plotted in Fig. 5.1 and Fig. 5.2 with comparisons to the original data by Werner and Meyer.

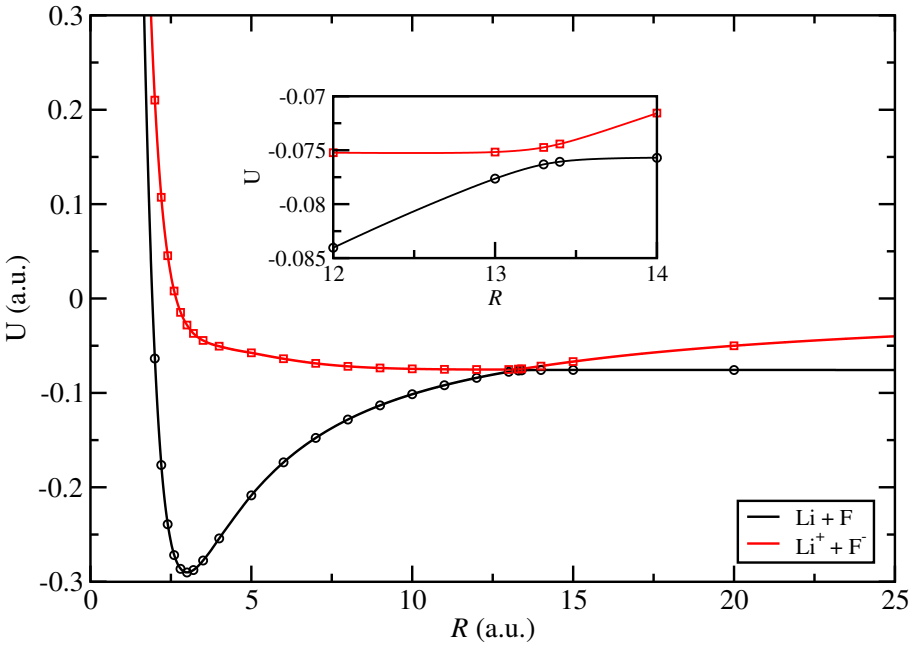

Figure 5.1: *Lowest two adiabatic potential energy curves for LiF. The symbols indicate values calculated by Werner and Meyer [1].*

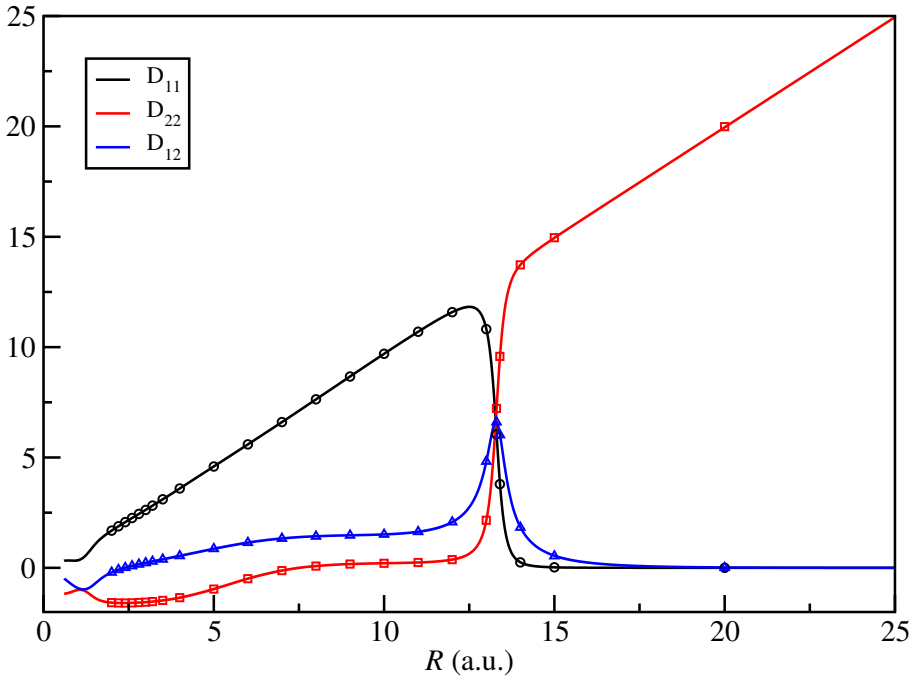

Figure 5.2: *Adiabatic dipole matrix elements as a function of R. The symbols indicate values calculated by Werner and Meyer.*

The transformation matrix, $\mathcal{U}$, can also be used to calculate the nonadiabtic coupling elements for the potentials we use. The first-order radial coupling terms, $\mathbf{P}$, have the general expression,

$$\mathbf{P} = \left\langle \mathbf{\Psi}_{\text{ad}} \left| \frac{d}{dR} \right| \mathbf{\Psi}_{\text{ad}} \right\rangle . \tag{5.5}$$

Applying the relation in Eq. (5.3) gives a simple expression for $\mathbf{P}$,

$$\mathbf{P} = \mathcal{U} \frac{d\mathcal{U}^{\dagger}}{dR}. \tag{5.6}$$

The result is a hollow, antisymmetric matrix for all values of R. The value of P_{12} is plotted as a function of R and compared to the Werner and Meyer values in Fig. 5.3.

The second-order radial coupling, $\mathbf{Q}$, is defined as

$$\mathbf{Q} = \left\langle \frac{d\mathbf{\Psi}_{\text{ad}}}{dR} \left| \frac{d\mathbf{\Psi}_{\text{ad}}}{dR} \right\rangle . \right. \tag{5.7}$$

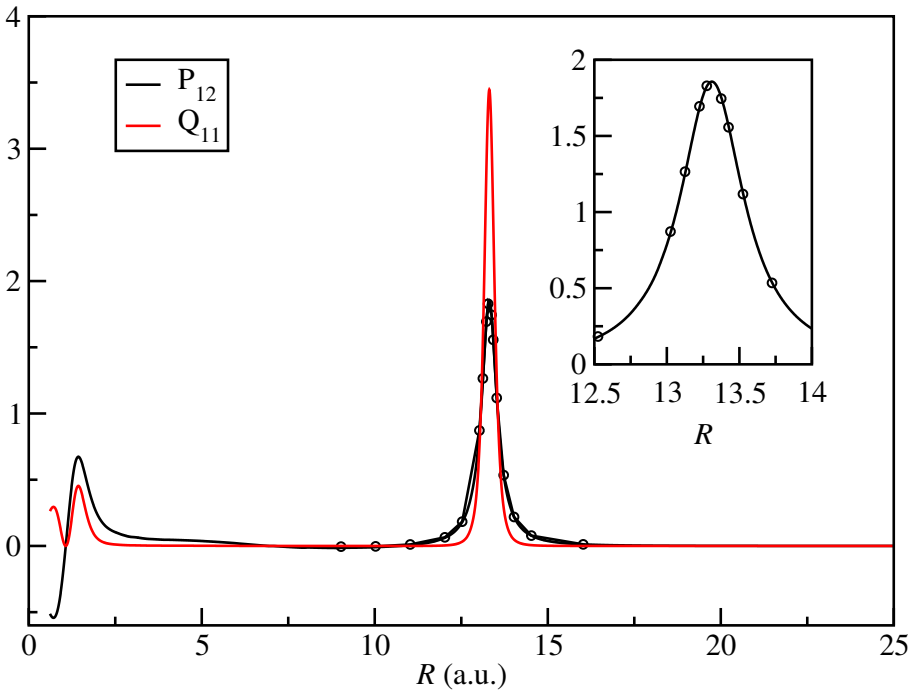

Figure 5.3: *Nonadiabatic coupling matrix elements, P_{12} (black line), and Q_{11} (red line) as a function of R. An enlarged plot of P_{12} around the main peak is shown in the inset. The symbols are values calculated by Werner and Meyer and are provided for comparison.*

Again, we apply the relation of Eq. (5.3) to obtain,

$$\mathbf{Q} = \frac{d\mathcal{U}}{dR}\frac{d\mathcal{U}^{\dagger}}{dR}. \tag{5.8}$$

The result is a diagonal matrix with its elements are plotted in Fig. 5.3, but no comparison is available since these elements were not calculated in original paper [1].

The nuclei used correspond to the most abundant isotopes, ^{7}Li and ^{19}F, with a mass of 12760 and 34634 atomic units, respectively. This yields a total of 125 vibrational states in the ground, adiabatic electronic potential with an energy separation on the order of 10^{-3} atomic units.

5.3 Scattering States

The calculation of the scattering states for the energy analysis is similar to what has been discussed in previous chapters, but the long-range behavior of the potentials differs from the HD^+ case. The potential for the lowest electronic channel, that corresponds to Li + F at large R, reaches a constant value very quickly as a function of R due to the R^{-6} behavior of the van der Waals potential. This means that the asymptotic form of the scattering wavefunction can be treated in the same way as done previously for HD^+. The other electronic channel, however, dissociates to $Li^+ + F^-$ meaning that the long-range behavior is described by a Coulomb potential. This long-range potential means that a standard plane wave is no longer an accurate representation of the asymptotic form of the radial wavefunction in the ionic channel. Fortunately, the solutions in a Coulomb potential are well known and can be expressed in terms of hypergeometric functions which are known as Coulomb functions. Following the formulation in Sec. 2.2, the regular and irregular Coulomb functions become f and g, respectively. The incoming, $f^{(-)}$, and outgoing, $f^{(+)}$, wavefunctions can then be expressed as the linear combination,

$$f^{(\pm)} = \sqrt{\frac{\mu}{\pi k}}\,(g \pm if)\,, \tag{5.9}$$

where k is the asymptotic momentum in the ionic channel. In the calculation, the Coulomb functions are evaluated numerically using a well-tested method [47]. From here, one only needs to follow the R-matrix formalism discussed in Sec. 2.4 to calculate the scattering states we desire.

5.4 Numerical Calculation

The calculation for LiF posses a numerical challenge if one wishes to maintain the same level of precision as previously achieved in HD^+. This is because the local wavelength of the wavefunction is much shorter, meaning that many more grid points are needed to accurately describe this function. Approximately 12000 grid points were needed in a grid that spans from $R = 1$–200 a.u. with a time step of 0.1 a.u. to achieve a minimum convergence of 3 digits in the energy spectrum and channel probabilities.

The method used to calculate the Coulomb functions needed for the energy analysis limits the value magnitude of kR to a maximum 1.96×10^4 atomic units. The maximum value of kR used in the calculations presented here was less than 10^4, so this problem does not impact our results. However, care must be taken if one wishes to expand the study of LiF to include fragmentation at larger kinetic energies or if one chooses to look at a heavier system that has a Coulomb potential.

5.5 Two-Color Delay Dependence

The formalism used to describe the carrier-envelope phase dependence in Ch. 4 can also be extended to give an analytical form for the two-color delay dependence in our observables. While we do not include nuclear rotation in our numerical calculations, it will be included in the following derivation to have a general formalism to work from. The connection to the case without rotation is the same as was described previously in Ch. 4 for the CEP dependence.

We begin by defining the electric field as

$$\mathcal{E}(t) = \mathcal{E}_1(t)\cos(\omega_1 t + \varphi) + \mathcal{E}_2(t)\cos[\omega_2(t - \tau_{\mathrm{tc}}) + \varphi], \tag{5.10}$$

where $\mathcal{E}_1(t)$ and $\mathcal{E}_2(t)$ are the envelopes of the fields, ω_1 and ω_2 are the central frequencies of the two pulses, φ is the carrier-envelope phase, and τ is the two-color delay. We note that the field is periodic in both φ and τ meaning that the Hamiltonian and wavefunction must also have the same periodicity. This allows us to expand the wavefunction in the series

$$\psi = \sum_{n,m} \psi_{n,m} e^{-i(n+m)\varphi} e^{im\omega_2 \tau_{\mathrm{tc}}}. \tag{5.11}$$

From Ref. [25], we learn that n and m describe the number of photons absorbed of frequency ω_1 and ω_2, respectively.

The dissociation probability as a function of angle, θ_k, and energy, E, can be expressed as,

$$\frac{\partial P^2}{\partial E \partial \theta_k} = \sum_{\substack{J,J' \\ n,n',m,m'}} A_{J,n,m}(E) A^*_{J',n',m'}(E) Y_{J0}(\theta_k) Y_{J'0}(\theta_k) e^{-i(n+m-n'-m')\varphi} e^{i(m-m')\omega_2 \tau_{\mathrm{tc}}}, \tag{5.12}$$

where

$$A_{J,n,m}(E) = \langle F_{J,k} | F_{J,n,m} \rangle \tag{5.13}$$

is the projection of the solution of the TDSE, after expansion using Eq. (5.11), onto the scattering state, $F_{J,k}$. An interpretation of $A_{J,n,m}(E)$ is that it describes the *pathway* the molecule took to dissociate where the value of $|A_{J,n,m}(E)|^2$ is the probability to dissociate with an energy, E, after absorption of n and m photons. Here, Y_{J0} are the spherical harmonics where the quantum number, M, is assumed to be zero. We can then integrate out θ_k to obtain

$$\frac{dP}{dE} = \sum_{\substack{J \\ n,n',m,m'}} A_{J,n,m}(E) A^*_{J,n',m'}(E) e^{-i(n+m-n'-m')\varphi} e^{i(m-m')\omega_2 \tau_{\mathrm{tc}}}. \tag{5.14}$$

The integration over θ_k forces $J = J'$ and restricts the values of $n + m$ and $n' + m'$ to have the same parity to satisfy the selection rule $\Delta J = \pm 1$ for the absorption or emission of one photon. This means that the quantity $n + m - n' - m'$ has even parity for all allowed values of n, n', m, and m'. The values of $m - m'$, however, have no such restriction. This means that the $\omega_2 \tau_{\mathrm{tc}}$ dependence of the energy distribution and yields can, in general, be a sum over all $m - m'$. In general, observables such as differential dissociation probability and total yields can be written in the series when $\varphi = 0$,

$$P = \sum_{m,m'} a_{m-m'} \cos\left[(m - m')\omega_2 \tau_{\mathrm{tc}} + \delta_{m-m'}\right]. \tag{5.15}$$

In practice, we may be able to reduce the terms in the summation in Eq. (5.14) by taking into account the fact that the photon pathways must overlap in energy in order to have any control with the two-color delay. This means that

$$(n - n')\omega_1 + (m - m')\omega_2 < \Delta E, \tag{5.16}$$

where ΔE is a parameter related to the width in energy of pathways $A_{J,n,m}(E)$ and $A_{J,n',m'}(E)$. In the perturbative limit where the dissociation probability is small, ΔE is directly proportional to the bandwidth of the laser pulse. In the multiphoton absorption regime, however, it becomes difficult to predict ΔE in a rigorous way. A more detailed discussion of relevant pathways is outlined later in Sec. 5.6.3.

5.6 Results and Discussion

5.6.1 Pump only

The role of the pump pulse is to generate a dissociating wave packet which is excited by a probe pulse at a later time. Knowing the characteristics of this wave packet is crucial for understanding the interaction with the probe. For this reason, the parameters of the pump are chosen such that the wave packet is created on the excited electronic channel from a one-photon absorption from the ground state in $v = 0$. This process is accurately calculated using our TDSE code and opens up the possibility for experimental realization in the future. Since only one photon is absorbed, the dissociating wave packet is expected to have properties that can be predicted by perturbation theory, meaning that the energy distribution has a simple dependence on the bandwidth of the pulse and the central frequency.

The electric field of the pump is given by

$$\mathcal{E}(t) = \mathcal{E}_0 e^{-\frac{t^2}{\tau^2}} \cos(\omega_0 t), \tag{5.17}$$

where the definitions of $\mathcal{E}_0$, τ, and ω_0 are the same as in previous chapters. The intensity of the pump is 10^{13} W/cm^2 with $\tau = 12$ fs and $\omega_0 = 0.3$ atomic units. The Coulomb potential of the ionic channel creates an infinity of resonant states for energies between the two thresholds. We wish to avoid any transitions to these states, so the central wavelength and pulse duration are chosen so that all energies of the initial dissociating wave packet are located above the highest threshold.

The energy distribution of the dissociating fragments on both the ionic and covalent channels is plotted in Fig. 5.4. The energy scale for this plot is the same as the vertical axis of Fig. 5.1; the threshold of the ionic channel is the zero of the plot. The location of the peak of the distribution and its Gaussian profile are consistent with what is expected from first-

order perturbation theory. The branching ratio of dissociation on the covalent channel is clearly dominant with 86 percent outgoing on this channel. The goal of the remaining work will be focused on finding a probe pulse that changes this branching ratio in a significant, controllable manner.

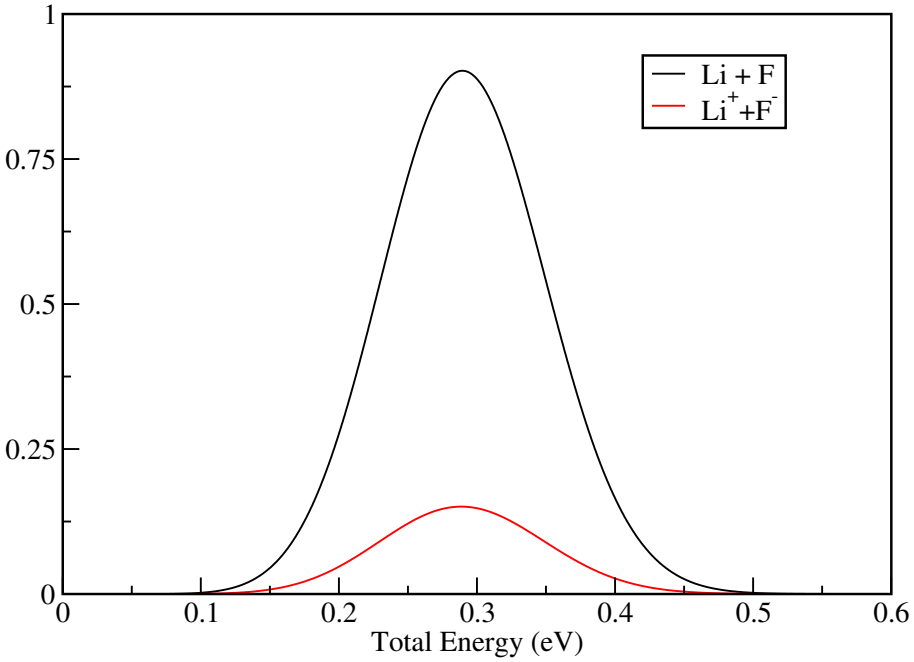

Figure 5.4: *Differential dissociation probability generated by the pump pulse.*

5.6.2 Pump with a Single-Color Probe

The peak in the transition dipole moment, D_{12}, at the avoided crossing, as seen in Fig. 5.2, suggests that applying a probe pulse when the dissociating wave packet is going through this region would give us the best chance to manipulate the branching ratios. The probe is expected to modify the branching ratios from the pump-only case in two possible ways: drive direct transitions from one channel to the other, or introduce additional dissociation pathways that end in the same electronic channel that then interfere. The form of the

electric field is,

$$\mathcal{E}(t) = \mathcal{E}_{\text{pump}}(t) + \mathcal{E}_{\text{probe}} e^{-\frac{(t-\Delta t)^2}{\tau'^2}} \cos(\omega' t)\,, \tag{5.18}$$

where $\mathcal{E}_{\text{pump}}(t)$ is the pump pulse described by Eq. (5.17), Δt is the pump-probe delay, τ' is the FWHM duration of the probe, and ω' is the frequency of the probe pulse.

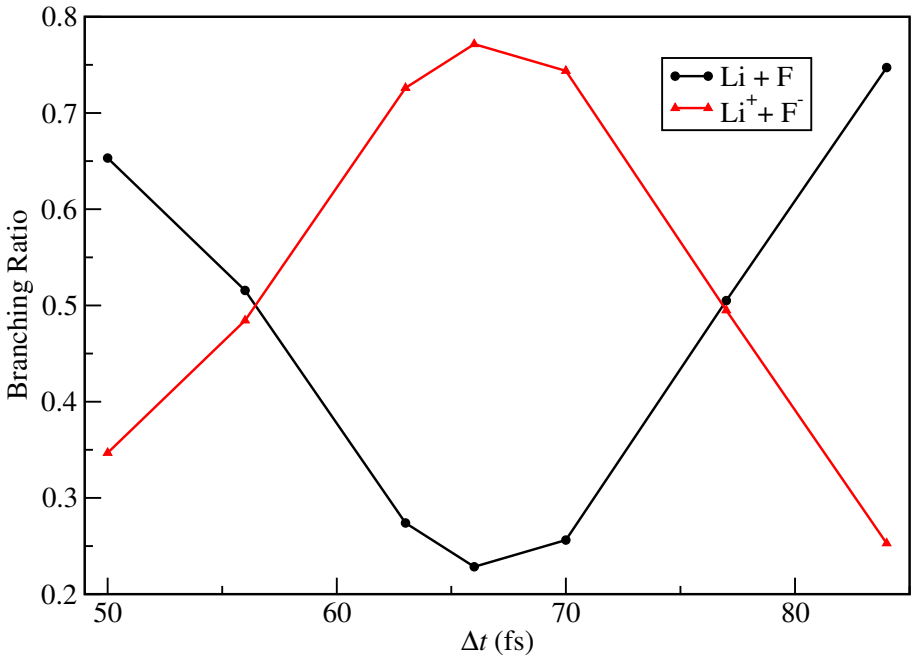

Figure 5.5: *Dissociation branching ratios as a function of* Δt.

The branching ratio of dissociation on the covalent channel as a function of delay is shown in Fig. 5.5 for a 800 nm, 15 fs probe pulse with a peak intensity of 10^{12} W/cm^2. The duration of the probe was chosen so that CEP effects could be neglected while keeping the bandwidth of the probe similar to the pump pulse. The effect of the probe on the branching ratios is significant with the dominant channel switching from the covalent channel to the ionic. The maximum change that occurs around a delay of 66 fs corresponds to the time the peak of the dissociating wave packet passes through the avoided crossing. This is determined by looking at the probability density during the time propagation with the pump only. This delay dependence implies that this is merely an intensity effect where delays longer or shorter

than $\sim$ 66 fs simply reduce the effective intensity the wave packet "feels" as it goes through the avoided crossing region.

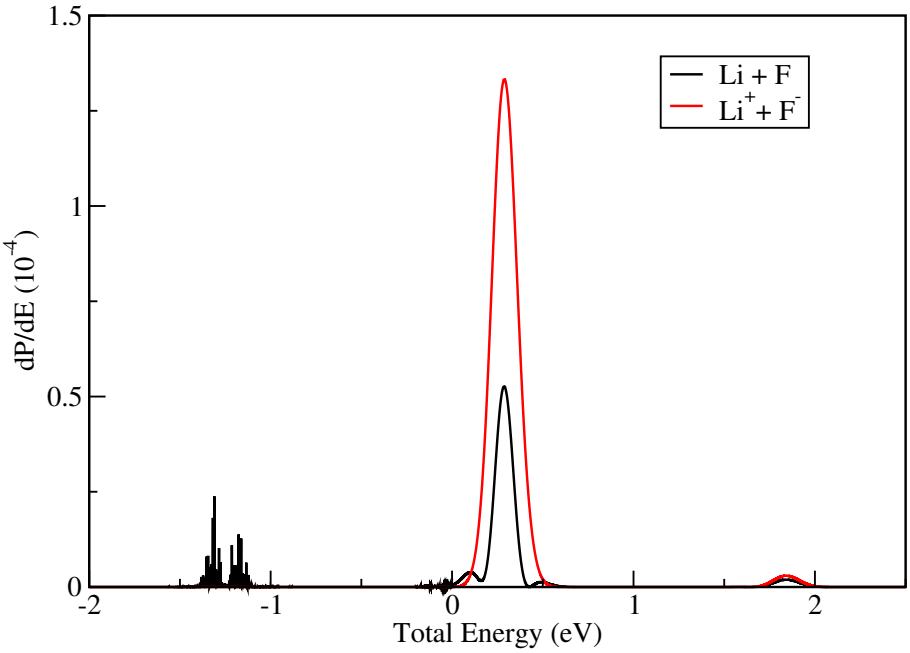

Figure 5.6: *Differential dissociation probability for a single-color, 800 nm, probe pulse with Δt =66 fs.*

In order to understand the mechanism that gives control over the branching ratios, we plot the energy distribution on both channels in Fig. 5.6 for the pump-probe case. The main peak of the distribution is located in a similar energy range as the pump-only shown in Fig. 5.4, but also has smaller side peaks corresponding to absorption or emission of one photon of the probe pulse. The small side peaks are evidence of a simple one-photon absorption that transfers population from one channel to the other; however, these peaks are relatively small compared to the main peak meaning that the direct-transfer process cannot be responsible for the change in the branching ratios we observe. The modulation of the main peak means that the control we find must come from the interference of at least two different dissociation pathways—one corresponding to only the pump and a multiphoton process that ends with zero net-photons absorbed. This is similar to the Raman-like process

described in Ch. 3 for the dissociation of HD^+. The interference between these pathways gives us the change in the branching ratio we observe. While this change in the branching ratios is significant, this scheme does not deviate far from the original experiments of Zewail and co-workers [2, 43]. We desire a control scheme that gives us more significant control over the branching ratios.

5.6.3 Pump with a Two-Color Probe

Control with a two-color laser pulse is a well-established technique that has shown considerable ability to manipulate the final products in a strong field [16, 48]. The basic idea is to control the interference between dissociation pathways that are produced by the different colors. The time delay between the two colors acts as the control knob by changing the phase difference between the pathways, thus influencing how they interfere. Historically, the colors used have been harmonics of each other because the pathways need to overlap in final energy to interfere, but we will take a different approach here. We will use the experience gained from the previous sections to design a scheme to gain more significant control over the branching ratios in comparison to the single-color probe case.

We take advantage of the result seen in the single-color probe case, that a Raman-like process is dominant, by choosing ω_1 and ω_2 to be be near 0.057 a.u. (800 nm). We learn that we want these processes to be large in magnitude and have considerable overlap to produce the most control. This gives us simple conditions to place on the laser parameters — the energy difference between the two colors and the width of the pump-only energy distribution must be roughly the same, the bandwidth of the pulses should be very similar, and the intensity of the probe should be sufficient that these pathways have a magnitude comparable or larger than the pump-only pathway.

The diagram shown in Fig. 5.7 illustrates the processes we intend to manipulate to give us control over the branching ratios. The lowest order control we can expect using the two-

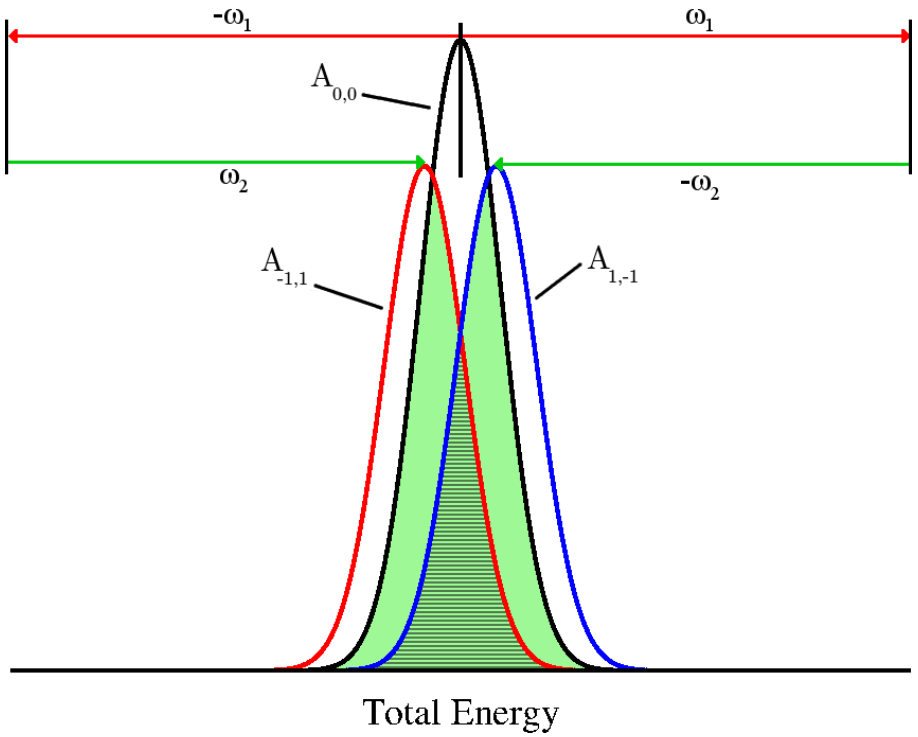

Figure 5.7: *Diagram showing the pathways we wish to generate to manipulate the branching ratios with the two-color probe. The green shading indicates interference giving* $\cos(\omega_2\tau)$ *dependence and the horizontal stripes indicate interference giving* $\cos(2\omega_2\tau)$ *dependence in the observables.*

color delay is from the interference between the pathways labeled $A_{0,0}$, $A_{1,-1}$, and $A_{-1,1}$. These are the same pathways described in the two-color formalism outlined in Sec. 5.5. Note that we have dropped the index corresponding to angular momentum, J, because we neglect rotation in our calculation. From Eq. (5.15), if these pathways are interfering in our calculation, we expect to see a $\cos(\omega_2\tau_{\rm tc})$ (green, shaded areas) and $\cos(2\omega_2\tau_{\rm tc})$ (horizontal stripes) dependence in our observables.

The electric field used is

$$\mathcal{E}(t) = \mathcal{E}_{\rm pump} + \mathcal{E}_2 e^{-\left(\frac{t'}{\tau_2}\right)^2} \left\{\cos\left(\omega_1 t'\right) + \cos\left[\omega_2\left(t' - \tau_{\rm tc}\right)\right]\right\}, \tag{5.19}$$

where $\mathcal{E}_{\rm pump}$ is the field of the pump given in Eq. (5.17), $\mathcal{E}_2$ is the peak field of the probe, τ_2

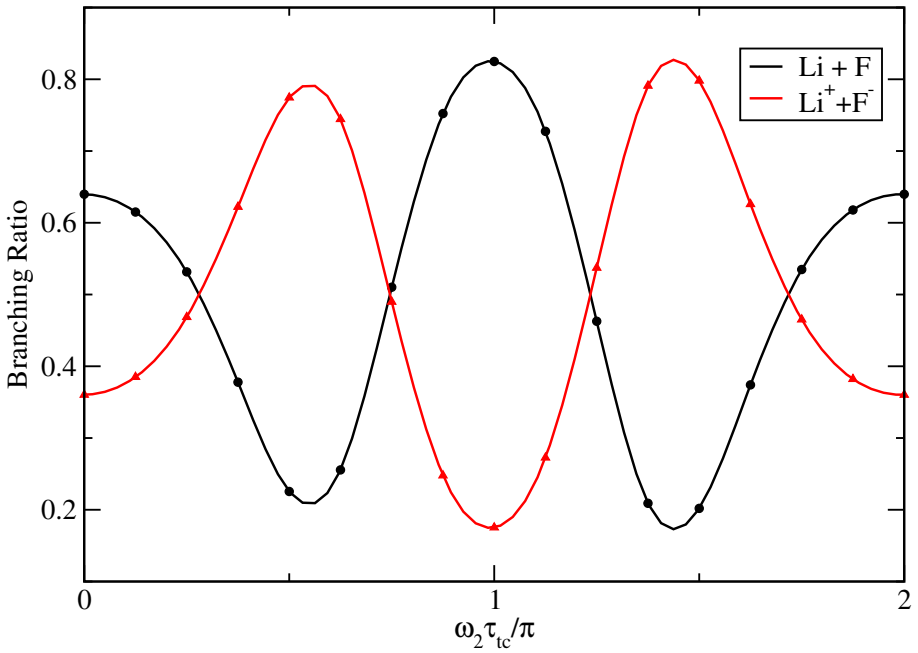

Figure 5.8: *Branching ratios of dissociation into Li + F (black lines) and $Li^+ + F^-$ (red lines) as a function of the delay between the two colors (789 nm and 811 nm) of the probe pulse with $\Delta t = 66$ fs.*

is the FWHM pulse duration, $t' = t - \Delta t$, ω_1 and ω_2 are the central frequencies of the two colors, and τ_{tc} is the delay between the two colors. The two colors used here correspond to wavelengths of 789 nm and 811 nm with both colors having an intensity of 10^{12} W/cm^2 and a pulse duration of 12 fs. We chose the pump-probe delay, Δt, to be 66 fs which corresponds to the maximum change in the branching ratios in the single-color probe case. In principle, the two colors used for this probe are within the bandwidth of the probe pulse used earlier in the single-color case. From this, we expect the level of control to be similar between the single and two-color probe cases, but more control parameters are available for the two-color probe.

The branching ratios as a function of τ_{tc} are plotted in Fig. 5.8. We find strong oscillations between the ionic and covalent channels where the ratio for a single channel oscillates by over sixty percent with τ_{tc}. For a small range of τ_{tc}, we find greater shift in the branching ratio than for the single-color case, but it is only improvement of a few percent. A discrete

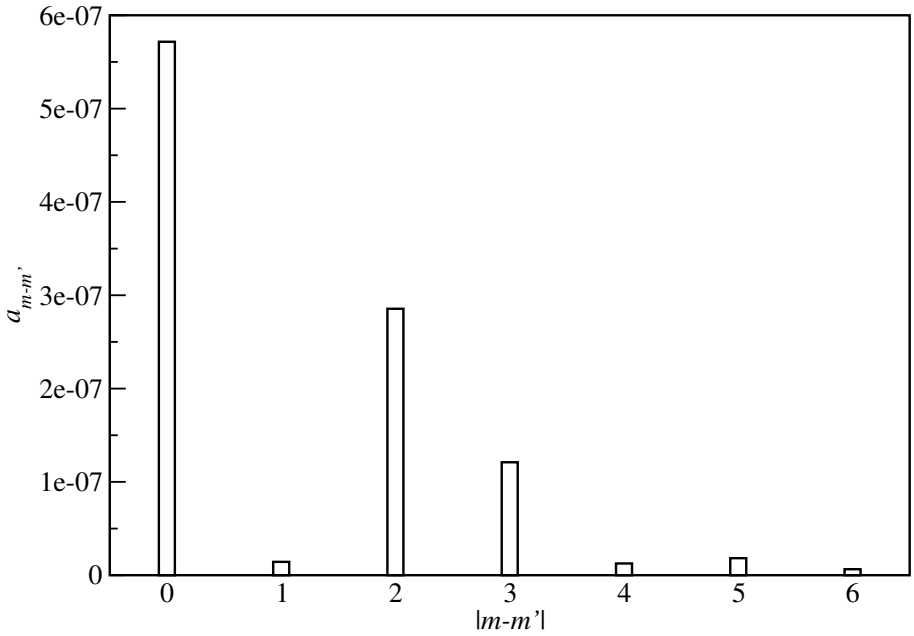

Figure 5.9: *Discrete Fourier transform of the dissociation yield on the covalent channel.*

Fourier transform of the dissociation yield in the covalent channel is provided in Fig. 5.9. We find that the branching ratio has oscillations of frequency $2\omega_2\tau_{\rm tc}$ which is consistent with our prediction using Fig. 5.7 and the theory described in Sec. 5.5, but the oscillations of frequency $\omega_2\tau_{\rm tc}$ are much smaller than what might be expected from our pathway picture where $\omega_2\tau_{tc}$-dependence would be the most dominant frequency. This suggests that the pathway, $A_{0,0}$, may be smaller than it appears in Fig. 5.7. In addition, we find considerable contribution from higher-order terms which is beyond the simple picture we sketched earlier.

The $\omega_2\tau_{\rm tc}$-dependent energy distribution for both electronic channels is plotted in Fig. 5.10. We choose to plot only the main features of the distribution that occur at energies around the threshold of the ionic channel. In Fig. 5.10(a), there is a localized peak in the distribution that corresponds to the maximum value of the covalent channel branching ratio seen in Fig. 5.8 which suggests a strong $\omega_2\tau_{\rm tc}$ dependence. However, at this same energy range we find two peaks in the distribution in the ion channel in Fig. 5.10(b) meaning that there is strong $2\omega_2\tau_{\rm tc}$ dependence as well. Clearly, we have multiple frequencies of $\omega_2\tau_{\rm tc}$ contributing

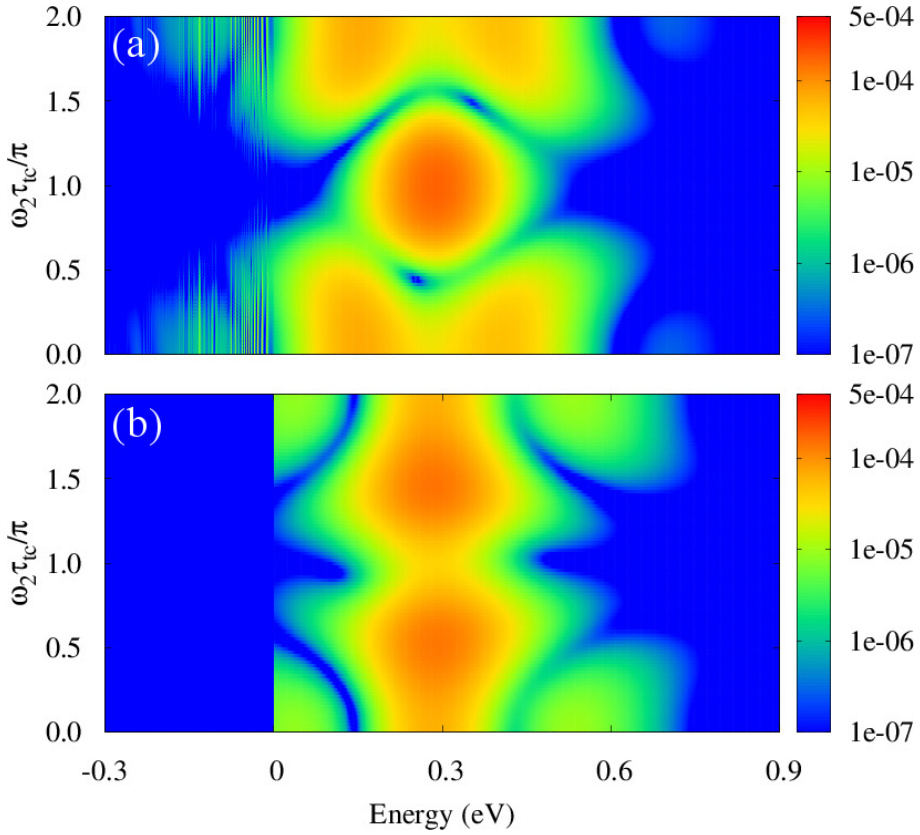

Figure 5.10: *Energy distribution for dissociation on the covalent channel (a), and ionic channel (b) as function of* $\omega_2\tau_{tc}$.

in a small energy range as described by the pathways shown in Fig. 5.7.

While we have developed a more sophisticated method, compared to the single-color probe scheme, of controlling the branching ratios using a two-color probe, the magnitude of the oscillations are no larger than what is achieved by a simple single-color probe as shown in Fig. 5.5 except for a small range of τ_{tc}. The laser parameters chosen here are not the only ones applicable to this system. More work needs to be done in order to see if this control scheme can be improved in a general way that can also be applied to other systems.

Chapter 6

Summary

The work presented in this thesis was focused primarily on controlling the final products in the dissociation of heteronuclear molecules in intense, femtosecond laser pulses. We began by presenting the general theory used to described these laser–molecule interactions where an adiabatic approximation was used to solve for the electronic motion, but additional nonadiabatic terms, that couple the electronic and nuclear degrees of freedom, are also included in the calculation.

Strong-field dissociation of the hydrogen molecular ion, HD^+, was the first subject studied in this thesis. The role of the permanent dipole was explored for laser wavelengths from 800 nm to 4000 nm. It was found that permanent dipole transitions had a large influence on the branching ratios, but had little impact on the total dissociation probability. This result was largely independent of the wavelength used. Plots of the energy spectrum using an 800 nm pulse suggest that the change in the branching ratio results from the dissociating wave packet making Raman-like transitions in the continuum. Further testing uncovered a complex relationship between electronic and permanent dipole transitions, and the nonadiabatic coupling that was unable to be described using a two-level model. More work is required if we wish to find a general explanation for the results we have observed. One

option is to use the photon-phase formlism discussed in Ch. 4 to break the wavefunction down into different net-photon components and use this to track the dissociation dynamics with more detailed information.

Control over the dissociation of HD^+ via the carrier-envelope phase (CEP) of the laser pulse was the next topic of study we presented. Here, we used two-cycle pulses for a few wavelengths between 800 nm and 4000 nm in order to find a general way to characterize the wavelength dependence of the strength of the CEP control we calculate. The results were analyzed using a previous established theory that gives an exact, explicit expression of the CEP dependence of the observables that comes from the interference between processes that have absorbed a different number of net photons. We find that, in general, wavelengths larger than 800 nm tend to produce larger— and higher-order—CEP dependence, but no simple wavelength dependence could be extracted from our calculations. By breaking the energy distribution down into its net-photon components via a Fourier transform in CEP, we find that the distribution has contributions from much higher-order terms than would be expected given the energy range of the original distribution. We found no general trend with the magnitude of the CEP oscillations and wavelength. This suggests that the relative bandwidth is not the only important parameter to keep fixed when trying to "normalize" the CEP dependence across many wavelengths. Finding the optimum "normalizing" parameter would give us a much better understanding of the dissociation dynamics that could then be applied to other systems.

We then moved on to study the dissociation dynamics of LiF using a pump-probe scheme. The relatively slow movement of the dissociating wave packet allows for the pump and probe to be well separated in time, making it easier to differentiate between effects caused by the pump and the probe. All calculations were performed with the same pump pulse to dissociate the molecule via a one-photon transition. The dissociating wave packet was then probed at a later time using both single-color and two-color laser pulses. In the single-color

pulse case, the branching ratios were controlled by the pump-probe delay where it was found that maximum control was achieved when the probe pulse was applied as the wave packet was traveling through the avoided crossing—where the dipole moments are the largest. In the two-color probe case, control was achieved via the delay between the two colors. The channel yields' dependence on this two-color delay can be expressed using the same, exact method used previously for CEP control in HD^+. While the two-color probe offers a more sophisticated control scheme that offers more control than the single-color probe, it gives only an increase of a few percent in the branching ratios. One possible improvement that could be made to our scheme would be to choose the two colors such that they are harmonics of each other. This would make it so the different photon pathways would have perfect overlap in energy, giving the possibility for better control of the branching ratios than we currently have.

A natural continuation of the work presented in this thesis is to perform the calculations with nuclear rotation included. Often, qualitative features found in systems without rotation carry over to a full calculation, but can be suppressed. One such case is the concept of vibrational trapping [49] that is overestimated in a calculation without rotation. This means we should be careful when we observe strong processes common to both molecules such as the Raman-like transitions in the continuum that appear to be responsible for much of the phenomena we studied. While there are valid concerns that appear by not including rotation, the work presented here serves as our first step to understanding the dynamics of these systems.

Bibliography

[1] H. Werner and W. Meyer, The Journal of Chemical Physics **74**, 5802 (1981), URL http://scitation.aip.org/content/aip/journal/jcp/74/10/10.1063/1.440893.

[2] T. S. Rose, M. J. Rosker, and A. H. Zewail, The Journal of Chemical Physics **88**, 6672 (1988), URL http://scitation.aip.org/content/aip/journal/jcp/88/10/10.1063/1.454408.

[3] A. Assion, T. Baumert, M. Bergt, T. Brixner, B. Kiefer, V. Seyfried, M. Strehle, and G. Gerber, Science **282**, 919 (1998), http://www.sciencemag.org/content/282/5390/919.full.pdf, URL http://www.sciencemag.org/content/282/5390/919.abstract.

[4] R. Kosloff, S. Rice, P. Gaspard, S. Tersigni, and D. Tannor, Chemical Physics **139**, 201 (1989), ISSN 0301-0104, URL http://www.sciencedirect.com/science/article/pii/0301010489900128.

[5] B. H. Bransden and C. J. Joachain, *Physics of Atoms and Molecules* (Pearson, 2003).

[6] B. D. Esry and H. R. Sadeghpour, Phys. Rev. A **60**, 3604 (1999), URL http://link.aps.org/doi/10.1103/PhysRevA.60.3604.

[7] V. Roudnev and B. D. Esry, Phys. Rev. A **76**, 023403 (2007), URL http://link.aps.org/doi/10.1103/PhysRevA.76.023403.

[8] M. Abu-samha and L. B. Madsen, Phys. Rev. A **82**, 043413 (2010), URL http://link.aps.org/doi/10.1103/PhysRevA.82.043413.

[9] F. Anis, Ph.D. thesis, Kansas State University (2009).

[10] N. P. Mehta, B. D. Esry, and C. H. Greene, Phys. Rev. A **76**, 022711 (2007), URL http://link.aps.org/doi/10.1103/PhysRevA.76.022711.

[11] B. Esry, Ph.D. thesis, University of Colorado (1997).

[12] E. Anderson, Z. Bai, C. Bischof, S. Blackford, J. Demmel, J. Dongarra, J. Du Croz, A. Greenbaum, S. Hammarling, A. McKenney, et al., *LAPACK Users' Guide* (Society for Industrial and Applied Mathematics, Philadelphia, PA, 1999), 3rd ed., ISBN 0-89871-447-8 (paperback).

[13] J. P. Boyd, *Chebyshev and Fourier spectral methods* (Courier Dover Publications, New York, 2001).

[14] X. Guan, O. Zatsarinny, K. Bartschat, B. I. Schneider, J. Feist, and C. J. Noble, Phys. Rev. A **76**, 053411 (2007), URL http://link.aps.org/doi/10.1103/PhysRevA.76.053411.

[15] M. Aymar, C. H. Greene, and E. Luc-Koenig, Rev. Mod. Phys. **68**, 1015 (1996), URL http://link.aps.org/doi/10.1103/RevModPhys.68.1015.

[16] A. Giusti-Suzor, F. H. Mies, L. F. DiMauro, E. Charron, and B. Yang, Journal of Physics B: Atomic, Molecular and Optical Physics **28**, 309 (1995), URL http://stacks.iop.org/0953-4075/28/i=3/a=006.

[17] J. H. Posthumus, Reports on Progress in Physics **67**, 623 (2004), URL http://stacks.iop.org/0034-4885/67/i=5/a=R01.

[18] E. Charron, A. Giusti-Suzor, and F. H. Mies, Phys. Rev. Lett. **75**, 2815 (1995), URL http://link.aps.org/doi/10.1103/PhysRevLett.75.2815.

[19] B. Sheehy, B. Walker, and L. F. DiMauro, Phys. Rev. Lett. **74**, 4799 (1995), URL http://link.aps.org/doi/10.1103/PhysRevLett.74.4799.

[20] J. Levesque, S. Chelkowski, and A. D. Bandrauk, Journal of Modern Optics **50**, 497 (2003), http://www.tandfonline.com/doi/pdf/10.1080/09500340308233546, URL http://www.tandfonline.com/doi/abs/10.1080/09500340308233546.

[21] A. Kondorskiy and H. Nakamura, Phys. Rev. A **66**, 053412 (2002), URL http://link.aps.org/doi/10.1103/PhysRevA.66.053412.

[22] J. McKenna, A. M. Sayler, B. Gaire, N. G. Johnson, M. Zohrabi, K. D. Carnes, B. D. Esry, and I. Ben-Itzhak, Journal of Physics B: Atomic, Molecular and Optical Physics **42**, 121003 (2009), URL http://stacks.iop.org/0953-4075/42/i=12/a=121003.

[23] A. Kiess, D. Pavičić, T. W. Hänsch, and H. Figger, Phys. Rev. A **77**, 053401 (2008), URL http://link.aps.org/doi/10.1103/PhysRevA.77.053401.

[24] R. Bhattacharya and S. S. Bhattacharyya, Phys. Rev. A **79**, 043415 (2009), URL http://link.aps.org/doi/10.1103/PhysRevA.79.043415.

[25] V. Roudnev and B. D. Esry, Phys. Rev. Lett. **99**, 220406 (2007), URL http://link.aps.org/doi/10.1103/PhysRevLett.99.220406.

[26] N. G. Kling, K. J. Betsch, M. Zohrabi, S. Zeng, F. Anis, U. Ablikim, B. Jochim, Z. Wang, M. Kübel, M. F. Kling, et al., Phys. Rev. Lett. **111**, 163004 (2013), URL http://link.aps.org/doi/10.1103/PhysRevLett.111.163004.

[27] T. Rathje, A. M. Sayler, S. Zeng, P. Wustelt, H. Figger, B. D. Esry, and G. G. Paulus, Phys. Rev. Lett. **111**, 093002 (2013), URL http://link.aps.org/doi/10.1103/PhysRevLett.111.093002.

[28] H. Xu, J.-P. Maclean, D. E. Laban, W. C. Wallace, D. Kielpinski, R. T. Sang, and I. V. Litvinyuk, New Journal of Physics **15**, 023034 (2013), URL http://stacks.iop.org/1367-2630/15/i=2/a=023034.

[29] H. Xu, T.-Y. Xu, F. He, D. Kielpinski, R. T. Sang, and I. V. Litvinyuk, Phys. Rev. A **89**, 041403 (2014), URL http://link.aps.org/doi/10.1103/PhysRevA.89.041403.

[30] M. F. Kling, C. Siedschlag, A. J. Verhoef, J. I. Khan, M. Schultze, T. Uphues, Y. Ni, M. Uiberacker, M. Drescher, F. Krausz, et al., Science **312**, 246 (2006), http://www.sciencemag.org/content/312/5771/246.full.pdf, URL http://www.sciencemag.org/content/312/5771/246.abstract.

[31] T. Pfeifer, A. Jullien, M. J. Abel, P. M. Nagel, L. Gallmann, D. M. Neumark, and S. R. Leone, Opt. Express **15**, 17120 (2007), URL http://www.opticsexpress.org/abstract.cfm?URI=oe-15-25-17120.

[32] M. Kübel, N. G. Kling, K. J. Betsch, N. Camus, A. Kaldun, U. Kleineberg, I. Ben-Itzhak, R. R. Jones, G. G. Paulus, T. Pfeifer, et al., Phys. Rev. A **88**, 023418 (2013), URL http://link.aps.org/doi/10.1103/PhysRevA.88.023418.

[33] J. J. Hua and B. D. Esry, Journal of Physics B: Atomic, Molecular and Optical Physics **42**, 085601 (2009), URL http://stacks.iop.org/0953-4075/42/i=8/a=085601.

[34] S. Chatterjee and S. S. Bhattacharyya, Phys. Rev. A **88**, 023408 (2013), URL http://link.aps.org/doi/10.1103/PhysRevA.88.023408.

[35] K. Liu, W. Hong, Q. Zhang, and P. Lu, Opt. Express **19**, 26359 (2011), URL http://www.opticsexpress.org/abstract.cfm?URI=oe-19-27-26359.

[36] P. Lan, E. J. Takahashi, and K. Midorikawa, Phys. Rev. A **86**, 013418 (2012), URL http://link.aps.org/doi/10.1103/PhysRevA.86.013418.

[37] I. Znakovskaya, P. von den Hoff, G. Marcus, S. Zherebtsov, B. Bergues, X. Gu, Y. Deng, M. J. J. Vrakking, R. Kienberger, F. Krausz, et al., Phys. Rev. Lett. **108**, 063002 (2012), URL http://link.aps.org/doi/10.1103/PhysRevLett.108.063002.

[38] K. Liu, Q. Zhang, P. Lan, and P. Lu, Opt. Express **21**, 5107 (2013), URL http://www.opticsexpress.org/abstract.cfm?URI=oe-21-4-5107.

[39] T.-Y. Xu and F. He, Phys. Rev. A **88**, 043426 (2013), URL http://link.aps.org/doi/10.1103/PhysRevA.88.043426.

[40] N. Ishii, K. Kaneshima, K. Kitano, T. Kanai, S. Watanabe, and J. Itatani, Nature Communications **5** (2013), URL http://dx.doi.org/10.1038/ncomms4331.

[41] G. Xu, S. F. Wandel, and I. Jovanovic, Review of Scientific Instruments **85**, 023102 (2014), URL http://scitation.aip.org/content/aip/journal/rsi/85/2/10.1063/1.4865132.

[42] W. H. Press, B. P. Flannery, S. A. Teukolsky, and W. T. Vetterling, *Numerical Recipes in Fortran 77: The Art of Scientific Computing* (Cambridge University Press, 1992), ISBN 052143064X.

[43] T. S. Rose, M. J. Rosker, and A. H. Zewail, The Journal of Chemical Physics **91**, 7415 (1989), URL http://scitation.aip.org/content/aip/journal/jcp/91/12/10.1063/1.457266.

[44] A. D. Bandrauk and J.-M. Gauthier, J. Opt. Soc. Am. B **7**, 1420 (1990), URL http://josab.osa.org/abstract.cfm?URI=josab-7-8-1420.

[45] M. Qing-Tian and A. J. C. Varandas, Chinese Physics B **22**, 073303 (2013), URL http://stacks.iop.org/1674-1056/22/i=7/a=073303.

[46] E. S. Rittner, The Journal of Chemical Physics **19**, 1030 (1951), URL http://scitation.aip.org/content/aip/journal/jcp/19/8/10.1063/1.1748448.

[47] A. Barnett, Computer Physics Communications **27**, 147 (1982), ISSN 0010-4655, URL http://www.sciencedirect.com/science/article/pii/0010465582900704.

[48] D. Ray, F. He, S. De, W. Cao, H. Mashiko, P. Ranitovic, K. P. Singh, I. Znakovskaya, U. Thumm, G. G. Paulus, et al., Phys. Rev. Lett. **103**, 223201 (2009), URL http://link.aps.org/doi/10.1103/PhysRevLett.103.223201.

[49] F. Anis and B. D. Esry, Phys. Rev. A **77**, 033416 (2008), URL http://link.aps.org/doi/10.1103/PhysRevA.77.033416.